UNIVERSITY OF COPENHAGEN
FACULTY OF SCIENCE

Master thesis

Quantifying the nature of compact objects

Geodesic synchrotron radiation from light rings

Tianyi Zhou

Supervisor: Prof. Dr. Vitor Cardoso

Submitted: May 22, 2023

Acknowledgements

First of all, I would like to express my sincere gratitude to my supervisor, Prof. Vitor Cardoso, for his guidance, patience and support during my thesis project. The same thanks go to Prof. Caio Macedo at Universidade Federal do Pará, who visited Copenhagen in 2022 and has been advising me on my thesis since then. I am also grateful for the opportunity to join the Strong Group at Niels Bohr Institute. You are all wonderful people!

I would also like to thank my parents, for the huge support throughout my life, and my girlfriend Han, for the love and companionship. It is my honour to have you in my life. I want thank my friends Yifei, Mu, Junqi, Jing and Zhengmao, as well as friends from Chaldea Security Organization and Rhodes Island Pharmaceutical Inc. You are the warm sunshine in the Nordic winter.

Finally, I would like to express my thanks to Lionel Andrés Messi as well as Argentina national football team, for always inspiring me to face tough times in life and to keep the faith never to give up.

Abstract

Black holes (BHs) are the simplest macroscopic objects predicted by Einstein's theory of General Relativity (GR). Nowadays, the concept of BH is widely used in astrophysics to refer to those densest astrophysical objects. However, the curvature singularity in the interior of BHs leads to breakdown of known physics. Exotic compact objects (ECOs) are proposed as BH mimickers and tightly connected with the dark matter puzzle. Therefore, using observations to quantify the nature of compact objects is of paramount importance. Predicted by GR, geodesic synchrotron radiation (GSR) has attracted attention again in recent years, providing approaches to probe spacetimes and the nature of ECOs.

Uniform-density stars are studied in this thesis as a proxy for ECOs due to its simplicity. A sufficiently compact uniform-density star can host two light rings, an unstable light ring in the exterior and a stable light ring in the interior, corresponding to circular null geodesics. Circular time-like geodesics are unstable when close to the unstable light ring, while circular time-like geodesics inside the stable light ring are stable. Charged particles can emit synchrotron radiation when orbiting on these circular time-like geodesics.

Scalar radiation in the vicinity of uniform-density stars is computed in both numerical and analytical approaches. Outside the star, scalar radiation has similar features to that in BH case: near the unstable light ring, the radiation is suppressed in each mode and dominated by high-frequency modes. It has also distinctive excitations due to those trapped modes. Inside the star, scalar radiation is suppressed when particles are close to the stable light ring, as well as when it is compared with the radiation emitted by particles orbiting the unstable light ring. Analytical result reveals that the suppression is due to the potential barrier between the stable light ring and turning point as the barrier corresponds to an exponentially decreasing factor. Less compact stars are expected to have lower potential barriers thus the suppression is less significant. Electromagnetic and axial gravitational radiation are also the same as those in BH case except for excitations. Radiations from the stable light ring are similarly suppressed.

Future work shall first investigate polar gravitational radiation for a complete understanding of GSR. Orbital evolution and gravitational waveform are also of interest. Other ECO models such as boson stars should also be considered and studied.

Contents

Chapter 1

Introduction

Black holes (BHs) are the simplest macroscopic objects predicted by Einstein's theory of General Relativity (GR). Back in 1915, Karl Schwarzschild derived the first static, spherically symmetric, vacuum solution to the field equations [1]. The solution with angular momentum was found in 1963 by Roy Kerr [2], which described a BH rotating at a constant angular velocity. In the context of astrophysics, it is straightforward to argue that any significant electric charge carried by BHs will be rapidly neutralized by surrounding plasma [3], as such BHs are described by only the mass M and the angular momentum J. This is a consequence to what is known as no-hair theorem [4].

Nowadays, more than one hundred years after the BH solution in GR was given, the concept of BH is widely applied in astrophysical research, referring to those densest astrophysical objects. In recent years, we have witnessed remarkable progress in the search for direct observational evidence of BHs, with the advent of gravitational wave astronomy [5–10] and very long baseline interferometry [11–22].

However, BHs also pose significant challenges to our understanding of physics. Non-rotating BHs are described by the Schwarzschild geometry (hereafter geometrical units $G = c = 1$ are used)

$$\mathrm{d}s^2 = -\left(1 - \frac{r_{\mathrm{H}}}{r}\right)\mathrm{d}t^2 + \left(1 - \frac{r_{\mathrm{H}}}{r}\right)^{-1}\mathrm{d}r^2 + r^2\left(\mathrm{d}\theta^2 + \sin^2\theta\mathrm{d}\phi^2\right). \tag{1.1}$$

There is a coordinate singularity at $r = r_{\mathrm{H}}$ that gives rise to the existence of an event horizon, which prevents us from probing the internal structure of a BH. This singularity can be eliminated through a coordinate transformation. Another singularity is located at $r = 0$. By constructing the Kretschmann scalar

$$\mathcal{K} = R_{\alpha\beta\gamma\rho}R^{\alpha\beta\gamma\rho} = \frac{12r_{\mathrm{H}}^2}{r^6}, \tag{1.2}$$

where $R_{\alpha\beta\gamma\rho}$ is the Riemann curvature tensor, we find the singularity at $r = 0$ is independent to our choice of coordinate thus a true curvature singularity, where the laws of

physics break down. We have to question whether other types of objects could exist that would exhibit similar behaviour as BHs.

A possible approach involves the concept of regular (i.e. non-singular) BH, which aim to resolve the issue by proposing modifications to BH, thereby avoiding the formation of the internal singularity (see [23] for a review). Generally, regular BHs are described by spherically symmetric, static and asymptotically flat metrics, which have non-singular centres. But they can still have horizons. A simple example is the Hayward metric [24], which introduces an additional parameter to measure the size of core region where the deviation from the Schwarzschild geometry becomes important. Due to the globality of the deviation, external probes such as gravitational lensing or shadow are possible, although the weak modifications are beyond the limits of current detection capabilities [25–27].

Exotic compact objects

An other possibility is the idea of exotic compact objects (ECOs, see [28] for a review), referring to horizonless compact objects other than neutron stars. ECOs are similar to BHs in some ways. Birkhoff's theorem ensures that the exterior of an isolated compact, spherically symmetric object is described by the Schwarzschild geometry (1.1), where $r_{\rm H} = 2M$ and M is the mass of the object. Therefore, geodesic motions outside ECOs are the same as those in vicinity of BHs. Circular time-like trajectories are stable for only $r \geqslant 6M$ and unstable for smaller radii. The innermost stable circular orbit (ISCO), defined at $r = 6M$, determines the size of the inner boundary of a geometrically thin accretion disk [29] and sets the upper limit for the characteristic frequency of compact emission regions ("hotspots") orbiting around accreting compact objects [30, 31].

The existence of circular null geodesics is another essential feature. A circular null geodesic is possible only at $r = 3M$ in the Schwarzschild geometry [32]. In an equatorial plane, it defines a light ring, which serves as a useful tool to understand compact objects. The circular null geodesic at $r = 3M$ is unstable, it defines a critical impact parameter. Photons from infinity with impact parameters below such a critical value will fall toward the compact object. Thus, the light ring actually determines how images of BHs or ECOs look like when they are illuminated by accretion disks or stars, defining their so-called shadow. On the other hand, consider the light ray emitted by a locally static source near the event horizon of a BH or the surface of an ECO at $r = r_0 \gtrsim 2M$, the escape angle $\psi_{\rm esc}$ is (see details in Appendix A)

$$\sin\psi_{\rm esc} = 3M\sqrt{3f_0}/r0, \tag{1.3}$$

where $f_0 = 1 - (2M/r_0)$. For angles larger than these, the light ray falls back and either gets absorbed by the event horizon of BH or hits the surface of the ECO, if there is

one. The light rays that are unable to escape reach a maximum coordinate distance $r_{\rm max} \sim 2M[1 + 4f_0M^2/(r_0^2 \sin^2 \psi)]$, where ψ is away from $\psi_{\rm esc}$. For $\psi \to \psi_{\rm esc}$, the $r_{\rm max}$ approaches the light ring at $r = 3M$. A non-zero escape angle indicates that radiation emitted near the surface of ECO can escape to infinity. As the escape angle vanishes in the $r_0 \to 2M$ limit, the ECOs with radii $\sim 2M$ can produce images extremely similar to BHs [33].

It is proved that if a spherically symmetric ECO has the necessary light ring to mimic a BH, it must also have a second, stable light ring , inside which circular time-like motions are stable [34–36]. Observational signatures related to such a stable light ring can therefore potentially serve as probes for ECOs. Figure 1.1 shows the general astrophysical environment hosting an ECO.

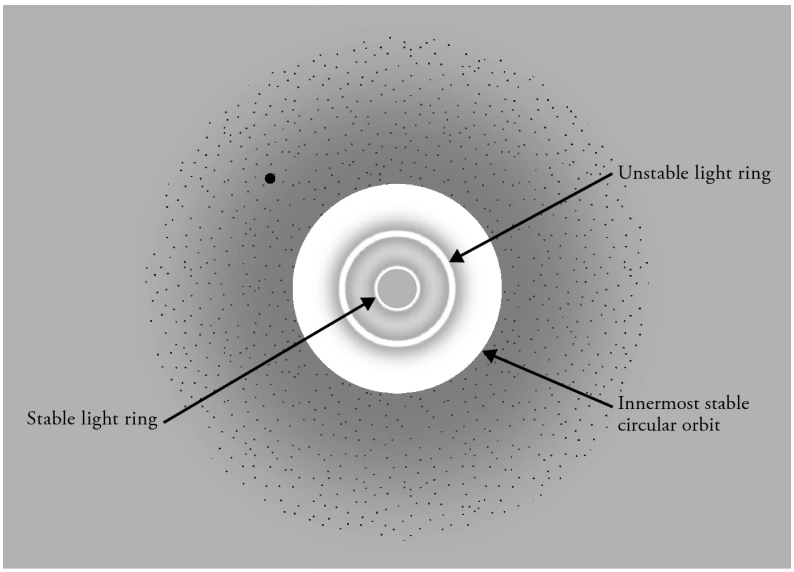

Figure 1.1: An equatorial slice of a very compact object. At large distances away from the center, physics is nearly Newtonian: other small objects – such as the small dot on the figure – can orbit on stable orbits. The external gray area is the entire region where stable circular motion is allowed. At the innermost stable circular orbit (ISCO), $r = 6M$, time-like circular motion is marginally stable. At the unstable light ring $r = 3M$, null geodesic motion is allowed. For horizonless objects, a second, stable light ring may exist as one approaches the geometric center. The astrophysical properties of a compact object depends on where in this diagram its surface is located. Figure is from [28].

The dark matter connection

The existence of dark matter (DM) has been discussed for more than a century [37–39], however the nature of DM remains unknown. Up to now, the evidence for DM is purely

gravitational. DM could be composed of different fields or particles, many of which are expect to form ECOs [40–42]. Thus, the signatures generated by ECOs consisting of DM have the potential to provide further clues.

One of the simplest examples is boson stars, arising from the self-gravitating solutions to minimally-coupled massive scalar field (see for a review). They can naturally form through gravitational collapse and may cluster around an ultracompact configuration via the process of "gravitational cooling" [43–46]. With the introduction of spin [47] or nonlinear interactions [35, 48, 49], boson stars can have light rings and ergoregions to mimic BHs. Due to their simplicity and fundamental nature, boson stars have attracted significant interest on addressing the DM puzzle [50].

As ECOs orbit around compact stellar objects, such as neutron stars or white dwarfs, their gravitational interactions can generate gravitational-wave signals. The system of ECOs and compact stars may exhibit unique dynamics. ECOs forming via gravitational collapse of DM can cluster around compact stars. Also, compact stars evolving in DM-rich environments may accrete a significant amount of DM in their interior [45]. These processes will leave their imprints on GW [51–53].

On another hand, BHs or ECOs can act as particle accelerators [54]. When a freely falling particle collides with a particle rest at the surface, their center-of-mass energy reads (see Appendix B for justification)

$$E_{\rm CM} = m_0\sqrt{2}\sqrt{1 - g_{\mu\nu}v^{\mu}_{(1)}v^{\nu}_{(2)}} \sim \frac{m_0\sqrt{2E}}{\epsilon^{\frac{1}{4}}}, \tag{1.4}$$

where $\epsilon = r_0/(2M) - 1$ and r_0 is the radius of the ECO surface. Therefore, even for small ϵ, the particles are relativistic. In the context of DM physics, such collisions can excite new degrees of freedom and yield detectable annihilation signals in gamma rays, high energy neutrinos or antiparticles [55].

Geodesic synchrotron radiation

Geodesic synchrotron radiation (GSR) is a phenomenon predicted by GR, in which charged point-like particles moving on a geodesic trajectory in the vicinity of a BH emit radiation. In the 1970s, it was considered an important observational target for the Weber gravitational wave telescope [56]. The scalar synchrotron radiation emitted by sources orbiting a Schwarzschild BH was first studied in [57]. Similar results have also been studied in electromagnetic and gravitational fields [58], which hold more realistic significance in astrophysics. It was shown that the GSR concept was not applicable in astrophysics, mainly due to the fact that it is unlikely to place particles stably near the photon orbits [59].

Recently, GSR has attracted attention again. Scalar synchrotron radiation is found to be strongly dependent on the cosmological constant in Schwarzschild-de Sitter spacetime [60]. Small BHs described by Schwarzschild-anti-de Sitter geometry shows different features on scalar synchrotron radiation from the Schwarzschild BHs [61]. Thanks to the Laser Interferometer Space Antenna (LISA) project [62], gravitational waves from extreme mass-ratio binaries, where smaller-mass objects are well approximated as point-like particles, is expected to be detected in the next decade [63]. The divergence in gravitational radiation emitted by particles orbiting the BH light ring is thus revisited and found to be curable [64].

ECOs can have the (unstable) light ring to mimic BHs. The study on GSR emitting by particles orbiting around ECOs is thus an inevitable step to understand the nature of ECOs. The existence of the second light ring results in the trapped, long-lived perturbations, possibly triggering the instability of ECOs [34]. Additionally, stable time-like orbits are allowed inside the stable light ring, providing a new channel to generate GSR. It seems unlikely that particles would be placed in geodesic orbits inside objects denser than neutron stars. But it can be possible in the presence of DM as their interaction with Standard Model particles is weak.

In this thesis, we study uniform-density stars as a proxy for ECOs. The idea of uniform-density stars dates back to the time when BH was first proposed [65], as a solution to the field equation describing a sphere of incompressible fluid with uniform density. It was later widely included in textbooks on GR (for example, [66–68]) and used in the study of neutron stars [69–72]. Due to its simplicity, uniform-density stars are also ideal models to investigate the properties of ECOs. Though there is an argument that the uniform-density stars do not exist in GR [73], the study of uniform-density stars should be sufficient to capture the main properties of ECOs.

Thesis outline

The rest of this thesis is structured as follows: In Chapter 2, we study null and time-like geodesics around uniform-density stars. In Chapter 3, we investigate geodesic synchrotron radiation produced by time-like particles orbiting near light rings, where we pay more attention to the stable light ring. This thesis is summarised in Chapter 4.

Chapter 2

Uniform-density stars

Uniform-density star is an ideal theoretical model to study the properties of ultra-compact astrophysical objects due to its simplicity. It assumes that the star has a uniform density throughout its interior. A uniform-density star with mass M can be described by a static, spherically symmetric spacetime with coordinates $\{t, r, \theta, \phi\}$ as

$$\mathrm{d}s^2 = -f(r)\mathrm{d}t^2 + \frac{1}{g(r)}\mathrm{d}r^2 + r^2\left(\mathrm{d}\theta^2 + \sin^2\theta\mathrm{d}\phi^2\right). \tag{2.1}$$

Outside the star, the spacetime is described by the Schwarzschild geometry, namely $f(r) = g(r) = 1 - (2M/r)$. Inside the star, the metric coefficients are given by [65–68]

$$f(r) = \frac{1}{4R^3}\left(\sqrt{R^3 - 2Mr^2} - 3R\sqrt{R - 2M}\right)^2, \tag{2.2}$$

$$g(r) = 1 - \frac{2Mr^2}{R^3}, \tag{2.3}$$

where R is the radius of the star. The pressure profile is given by

$$P(r) = \rho\frac{\left(1 - \frac{2Mr^2}{R^3}\right)^{\frac{1}{2}} - \left(1 - \frac{2M}{R}\right)^{\frac{1}{2}}}{3\left(1 - \frac{2M}{R}\right)^{\frac{1}{2}} - \left(1 - \frac{2Mr^2}{R^3}\right)^{\frac{1}{2}}}, \tag{2.4}$$

where $\rho = 3M/(4\pi R^3)$ is the density of the star. Its central pressure is

$$P_c = \rho\frac{1 - \left(1 - \frac{2M}{R}\right)^{\frac{1}{2}}}{3\left(1 - \frac{2M}{R}\right)^{\frac{1}{2}} - 1}. \tag{2.5}$$

A finite central pressure requires

$$3\left(1 - \frac{2M}{R}\right)^{\frac{1}{2}} - 1 > 0, \tag{2.6}$$

thus

$$\frac{M}{R} < \frac{4}{9}. \tag{2.7}$$

This bound is also known as the Buchdahl bound, the maximum compactness that a stable, spherically symmetric object can have without collapsing to a BH [74].

2.1 Null geodesics

For geodesic motion, the Lagrangian is given by

$$2\mathcal{L} = -f(r)\dot{t}^2 + \frac{\dot{r}^2}{g(r)} + r^2\left(\dot{\theta}^2 + \dot{\phi}^2\sin^2\theta\right) = -\delta, \tag{2.8}$$

where $\delta = 0$ for null geodesics and $\delta = 1$ for time-like geodesics. Consider the geodesics in the equatorial plane $\theta = \pi/2$ and $\dot{\theta} = 0$, the radial equation is

$$\frac{f(r)}{g(r)}\dot{r}^2 = E^2 - L^2 f(r)\left(\frac{1}{r^2} + \frac{\delta}{L^2}\right). \tag{2.9}$$

The constants of motion are defined by

$$E = -\frac{\partial\mathcal{L}}{\partial\dot{t}} = f(r)\dot{t}, \tag{2.10}$$

$$L = \frac{\partial\mathcal{L}}{\partial\dot{\phi}} = r^2\dot{\phi}, \tag{2.11}$$

where E and L are energy and angular momentum of the photon or specific energy and angular momentum of the time-like particle, respectively.

For the equatorial null geodesics, Eq.(2.9) becomes

$$\frac{f(r)}{g(r)}\dot{r}^2 = L^2\left[\frac{1}{b^2} - V_{\rm null}(r)\right], \tag{2.12}$$

where $V_{\rm null}(r) = f(r)/r^2$ is the null geodesic potential, and $b = L/E$ is the impact parameter. A circular geodesics not only indicates that $\dot{r} = 0$, but also that equilibrium is reached in the r direction, thus $V'_{\rm null}(r) = 0$. The radii of possible circular null geodesics are obtained by solving

$$V'_{\rm null}(r) = \frac{rf'(r) - 2f(r)}{r^3} = 0. \tag{2.13}$$

Outside the star, the solution to Eq.(2.13) is $r = r_+ \equiv 3M$, known as the unstable light ring for a Schwarzschild BH due to $V''_{\rm null}(r_+) < 0$. Inside the star, the solution to Eq.(2.13) is

$$r = r_- \equiv \sqrt{\frac{R^3(4R - 9M)}{9M(R - 2M)}}, \tag{2.14}$$

which tends to zero in the Buchdahl limit $R \to 9M/4$. Since

$$V''_{\rm null}(r_-) = \frac{M}{R^3}\left[\frac{81(R - 2M)^2}{R^2} - 1\right] > 0, \tag{2.15}$$

the circular null geodesics at $r = r_-$ correspond to a second, but stable, light ring. To better mimic Schwarzschild BHs, we demand $M/R > 1/3$, otherwise there is no light ring,

which is an important observational signature for quantifying BHs. Moreover, $M/R > 1/3$ leads to $r_- < R$ so that the stable light ring exists inside the star. Therefore, only those uniform-density stars with compactness

$$\frac{1}{3} < \frac{M}{R} < \frac{4}{9} \tag{2.16}$$

will be considered hereafter. Figure 2.1 shows the potential $V_{\rm null}(r)$ of uniform-density stars with various compactness values. In the critical case $R = 3M$, $r_+ = r_- = 3M$, the stable and unstable light rings overlap and become an unstable light ring.

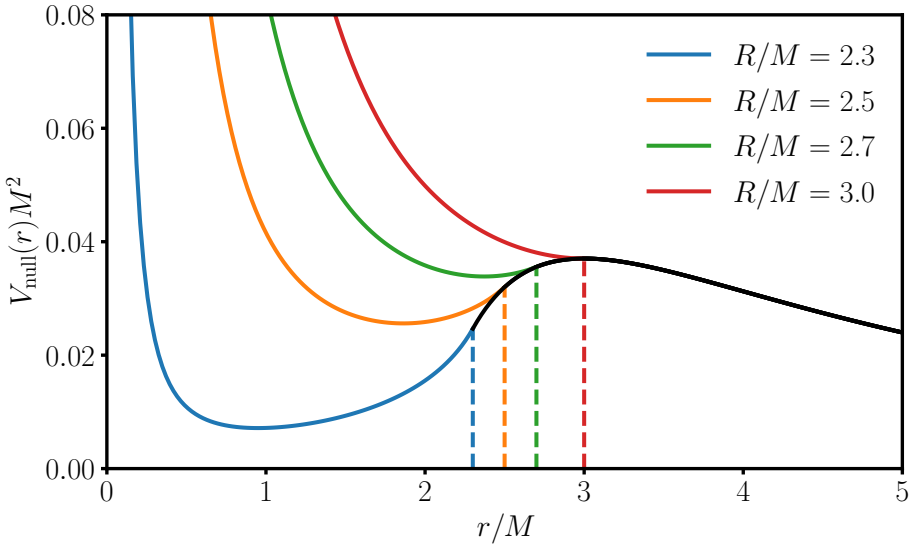

Figure 2.1: Curves of the potential $V_{\rm null}(r)$ with various compactness values. The colored solid lines show null geodesic potential curves in the interior of uniform-density stars, while the black solid line shows the exterior. The vertical colored dashed lines correspond the positions of star surfaces. For $R < 3M$, there is a local minimum of the potential at r_-, corresponding to the stable light ring inside the star, and a local maximum at r_+, corresponding to the outside unstable light ring. In the critical case $R = 3M$, two light rings overlap and become an unstable light ring.

2.1.1 Unbound photon orbits

Outside the star, the local maximum of null geodesic potential is $V_{\rm null}(r_+) = 1/(27M^2)$. For photons from infinity with $b > 1/\sqrt{V_{\rm null}(r_+)} = 3\sqrt{3}M \equiv b_+$, according to Eq.(2.12), $\dot{r}^2$ decreases to zero before the photons reach r_+. Therefore, photons from infinity with $b > b_+$ cannot enter the outside unstable light ring due to the potential barrier. These photons will be deflected and travel toward infinity. For the critical case $b = b_+$, the

photon will approach the unstable light ring and stay on it for infinite time. This is exactly the same as how it travels when approaching a Schwarzschild BH.

Photons with $b < b_+$ are able to pierce the star, if nothing inside the star interacts with photons. This allows the observers at infinity to capture photons from the surface or interior of the star, which is impossible for a Schwarzschild BH. Figure 2.2 shows examples of trajectories of photons from infinity with $b < b_+$.

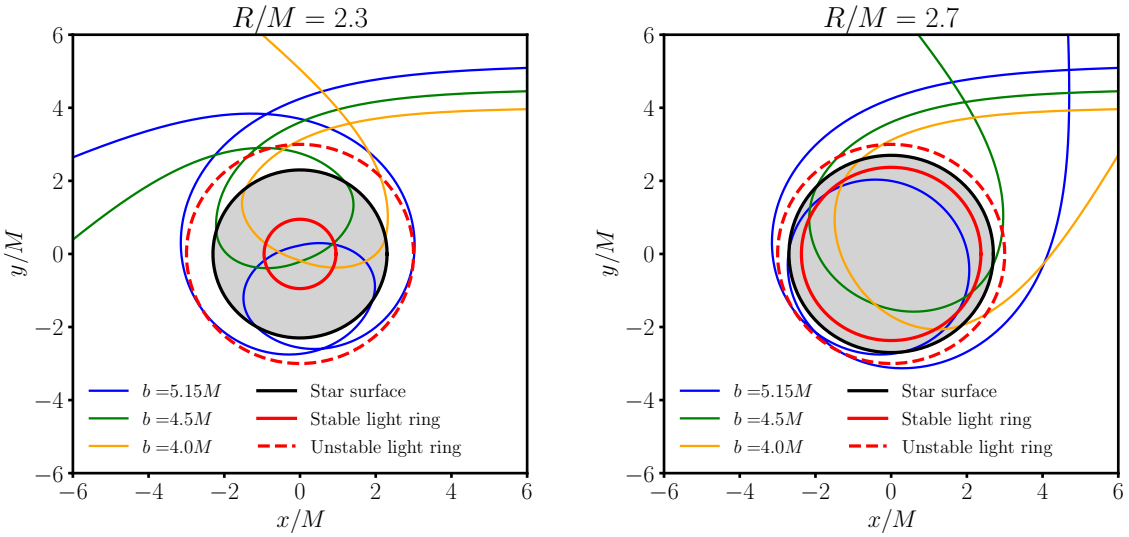

Figure 2.2: Trajectories of photons from infinity with impact parameter $b < b_+ \approx 5.20M$ in the spacetime of a uniform-density star. Radii of stars are $2.3M$ (*left*) and $2.9M$ (*right*). The grey area shows the inner region of the star. Under the assumption that photons do not interact with the stellar matter, these photons can pierce the star. For a fixed impact parameter, the scattering angle is larger for more compact stars.

2.1.2 Bound photon orbits

Differing from the Schwarzschild BH, the local minimum of null geodesic potential allows to trap photons inside the unstable light ring, even inside the star, corresponding to bound photon orbits. The lower limit of impact parameter of a trapped photon is $b_+ = 3\sqrt{3}M$. The critical case $b = b_+$ now corresponds to a photon staying on the unstable light ring for an infinite time before falling to the central region of the star. As the impact parameter increases, photon orbits shrink. Apocenters of photon orbits become farther from the unstable light ring and closer to the star surface before photons are completely trapped inside the star. So there is a critical value of impact parameter b_R making apocenters just located on the star surface, which satisfies with $\dot{r}^2|_{r=R} = 0$, thus

$$b_R = \frac{R^2}{\sqrt{R(R-2M)}}. \tag{2.17}$$

If the impact parameter continues increasing, the orbit gets closer to the stable circular orbit, namely the stable light ring. The maximum impact parameter is thus obtained by $\dot{r}^2|_{r=r_-} = 0$ as

$$b_- = \frac{R^2}{\sqrt{(4R-9M)M}}. \tag{2.18}$$

The orbit with $b > b_-$ is not allowed inside the star since $\dot{r}^2$ becomes negative. In Figures 2.3 and 2.4 we find photon trajectories with $b_+ < b < b_R$ clearly show the zoom-whirl behaviour described in [75], while photon trajectories with $b_R < b < b_-$ seem to be closed. Following [75], a bound photon orbit can be described by a unique number q as

$$q = \frac{\Delta\phi}{2\pi} - 1, \tag{2.19}$$

where $\Delta\phi$ is the accumulated azimuth between successive pericenter during a whole radial period and is given by

$$\Delta\phi = 2\int_{r_{\rm peri}}^{r_{\rm apo}} \frac{\mathrm{d}\phi}{\mathrm{d}r}\,\mathrm{d}r, \tag{2.20}$$

where $r_{\rm apo,peri}$ are two turning points of the bound orbit, obtained by setting $\dot{r}^2 = 0$. When q is a rational number, the photon travels in a periodic orbit and return to its initial position exactly after a finite timespan. Otherwise, the orbit will precess when q is irrational.

Figure 2.5 displays q as a function of impact parameter b for various values of the star's compactness. Within the range of (b_+, b_R), q decreases from infinity to zero. For the impact parameter $b > b_R$, numerical calculation returns negligible results of q, indicating that $q = 0$ and all the orbits are closed. More details are revisited in Appendix C.

2.2 Time-like geodesics

As we have studied null geodesics in the uniform-density star geometry, here we shall study the circular time-like geodesics in such a geometry, which will be useful in our following study.

For the equatorial time-like geodesics, Eq.(2.9) becomes

$$\frac{f(r)}{g(r)}\dot{r}^2 = E^2 - L^2 V_{\rm tl}(r), \tag{2.21}$$

where

$$V_{\rm tl}(r) = f(r)\left(\frac{1}{L^2} + \frac{1}{r^2}\right). \tag{2.22}$$

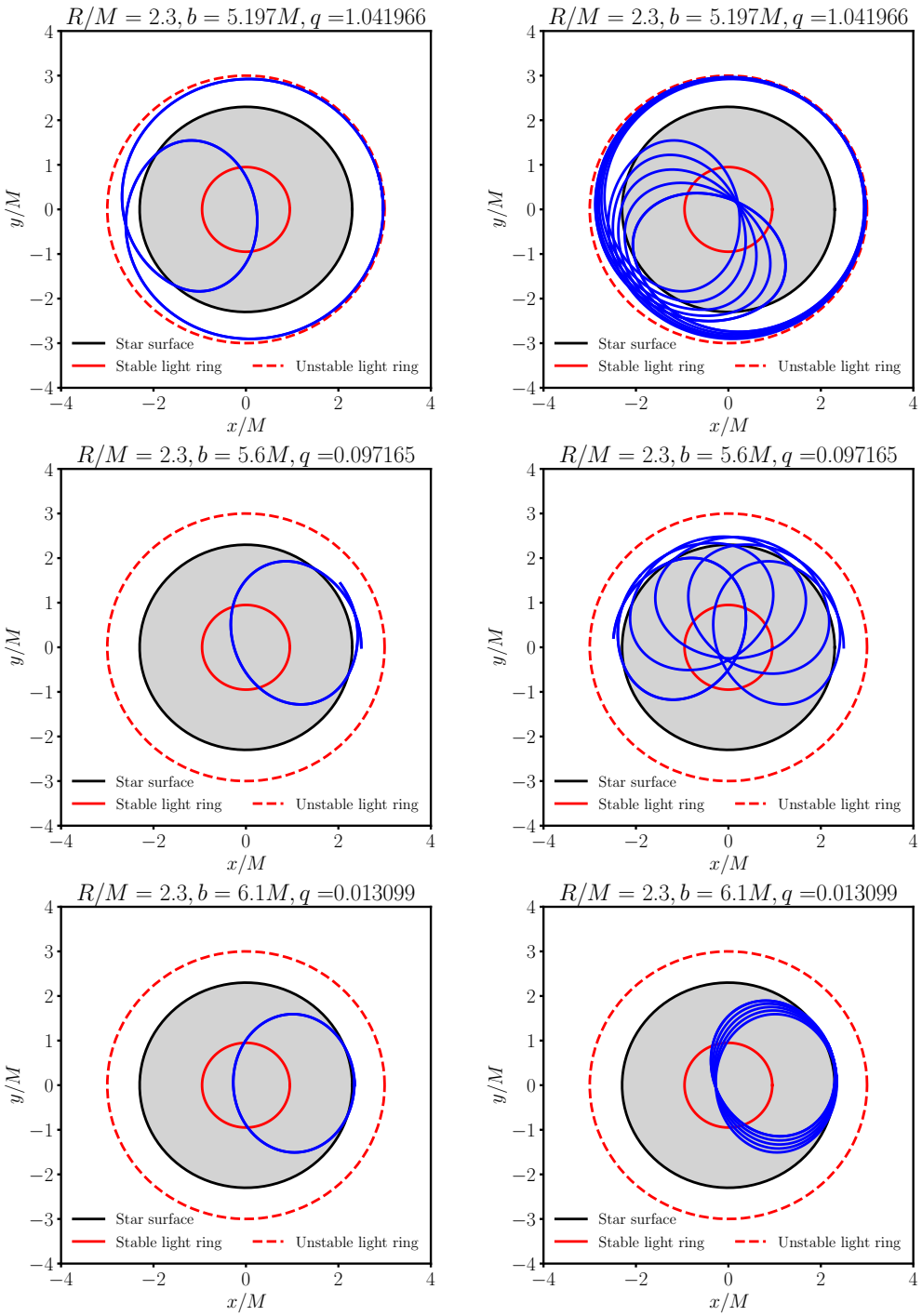

Figure 2.3: Trajectories of photons trapped in the unstable light ring, with $b_+ < b < b_R$. The radius of the star is fixed as $R = 2.3M$. Solid black circle corresponds to the star surface, while solid and dashed red circles respectively correspond to stable and unstable light rings. The grey area shows the inner region of the star. In the left column, only one radial period for each orbit is displayed. In the right column, five radial periods are displayed, where orbital precession and zoom-whirl behaviour are obvious.

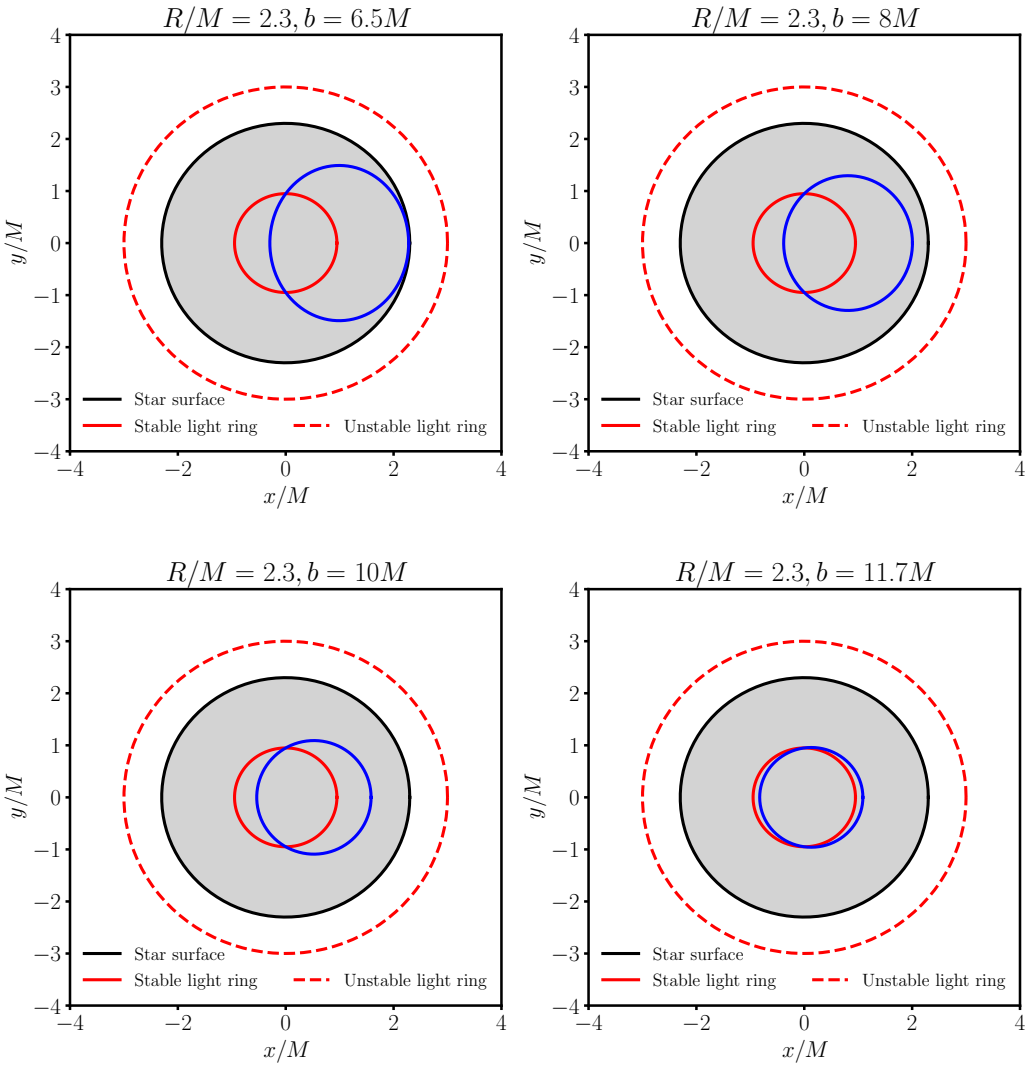

Figure 2.4: Trajectories of photons trapped in the uniform-density star, with $b_R < b < b_-$. The radius of the star is fixed as $R = 2.3M$. Solid black circle corresponds to the star surface, while solid and dashed red circles respectively correspond to stable and unstable light rings. The grey area shows the inner region of the star. All the orbits inside the star are found to be closed ($q = 0$).

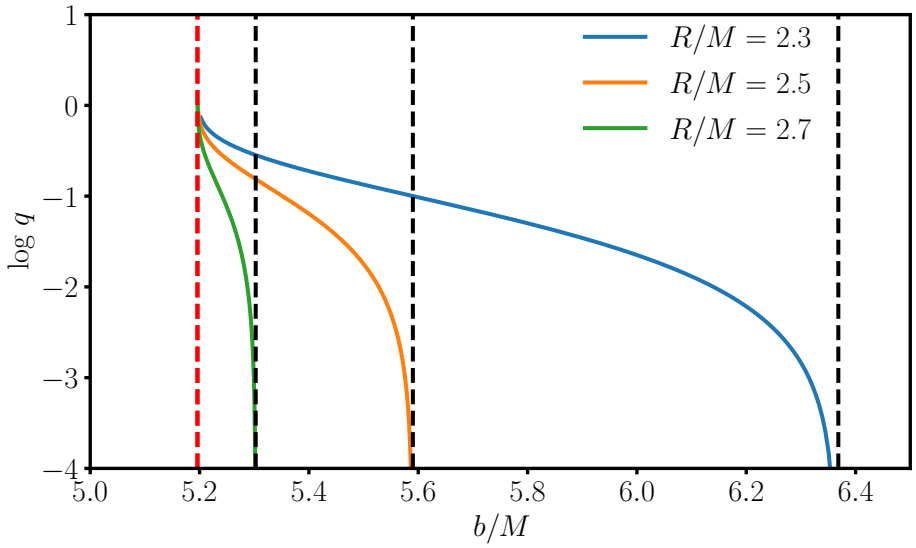

Figure 2.5: q as a function of impact parameter b, for various values of the star's compactness. Red dashed line corresponds to b_+, while black dashed lines correspond to b_R. q decreases from infinity to zero in (b_+, b_R), and $q = 0$ in $b > b_R$, indicating all the orbits bounded inside the star are closed.

For circular motions at $r = r_{\rm p}$, we have $\dot{r} = 0$. Demanding $V'_{\rm tl}(r_{\rm p}) = 0$, we obtain

$$L^2 = \frac{r_{\rm p}^3 f'(r_{\rm p})}{2f(r_{\rm p}) - r_{\rm p} f'(r_{\rm p})}. \tag{2.23}$$

Inserting Eq.(2.23) into Eq.(2.21) and setting $\dot{r} = 0$, we have

$$E^2 = \frac{2f^2(r_{\rm p})}{2f(r_{\rm p}) - r f'(r_{\rm p})}, \tag{2.24}$$

which leads to

$$\left(u^t_{\rm p}\right)^2 = \left[\frac{E}{f(r_{\rm p})}\right]^2 = \frac{2}{2f(r_{\rm p}) - r f'(r_{\rm p})}, \tag{2.25}$$

$$\Omega^2_{\rm p} = \left(\frac{{\rm d}\phi}{{\rm d}t}\right)^2 = \frac{f'(r_{\rm p})}{2r_{\rm p}}, \tag{2.26}$$

where $u^t_{\rm p}$ is the t-component of four-velocity and $\Omega_{\rm p}$ is the orbital frequency. A positive L^2 requires that

$$r_{\rm p} > 3M = r_+, \text{ for } r > R; \tag{2.27}$$

$$r_{\rm p} < \sqrt{\frac{R^3(4R - 9M)}{9M(R - 2M)}} = r_-, \text{ for } r < R. \tag{2.28}$$

Therefore, circular time-like geodesics are only allowed either outside the unstable light ring at r_+ or inside the stable light ring at r_-. Outside the star, we find

$$V''_{\rm tl}(r_{\rm p}) = \frac{2M^2(r_{\rm p}-6M)}{r_{\rm p}^5}, \tag{2.29}$$

implying that for $r_{\rm p} > 6M$ the circular orbits are stable and at $r_{\rm p} = 6M$ the circular orbit is marginally stable. Inside the star, we find

$$V''_{\rm tl}(r_{\rm p}) = \frac{6f(r_{\rm p})}{r_{\rm p}^4} - \frac{4f'(r_{\rm p})}{r_{\rm p}^3} + \frac{2f(r_{\rm p})f''(r_{\rm p})}{r_{\rm p}^3 f'(r_{\rm p})}. \tag{2.30}$$

Its full expression is rather complex. Numerical result shows that $V''_{\rm tl}(r_{\rm p}) > 0$ within $R/M \in (9/4, 3)$ and $r_{\rm p} \in (0, r_-)$. Therefore all circular time-like orbits are stable inside the stable light ring.

Figure 2.6 shows the angular momentum L, energy E of circular time-like geodesics and their ratio L/E as a function of orbital radius $r_{\rm p}$, for different compactness of stars. Both L and E diverge at $r_{\rm p} \to r_-$ and their ratio tends to the light-ring impact parameter b_-.

In the Section 2.1.2, it has been shown that null geodesics trapped inside the star are closed. Here we check whether this also applies to time-like geodesics. Consider those time-like geodesics inside the stars, for any given L, there is a particular range for allowed energy. The minimum energy $E_{\rm min}$ is determined by the circular orbit with the given L, solved from the combination of Eqs.(2.23) and (2.24). The maximum allowed energy $E_{\rm max}$ corresponds to the orbit tangent to the star surface, i.e. $E^2_{\rm max} = L^2 V_{\rm tl}(R)$. In Figure 2.7, we plot the allowed energy range against L, with various compactness of stars. The energy range becomes narrow for less compact stars. Figure 2.8 displays how the value of q changes against L and E. The energy is normalized by introducing

$$\eta = \frac{E - E_{\rm min}}{E_{\rm max} - E_{\rm min}}. \tag{2.31}$$

Note that all values of q are non-zero, indicating that all the time-like orbits are precessional. The only closed time-like orbits are circular ones, otherwise q changes slowly against energy for a given L. Also, we note that q-values are tiny at large energy limits since time-like particles exhibit behaviours similar to photons.

Due to the lack of horizon and the assumption that the stellar matter does not interact with the particles, time-like particles are allowed to stably travel between the stable and unstable light rings, as shown in Figure 2.9, which differs from the scenario of photons: photons either leave the unstable light ring outwards to infinity, or get trapped inside it. Furthermore, for a less compact star, it is allowed that particles orbit from near the outside light ring to the inside light ring, thus emit radiation on both circular-like orbits near the outside light ring and the inside light ring.

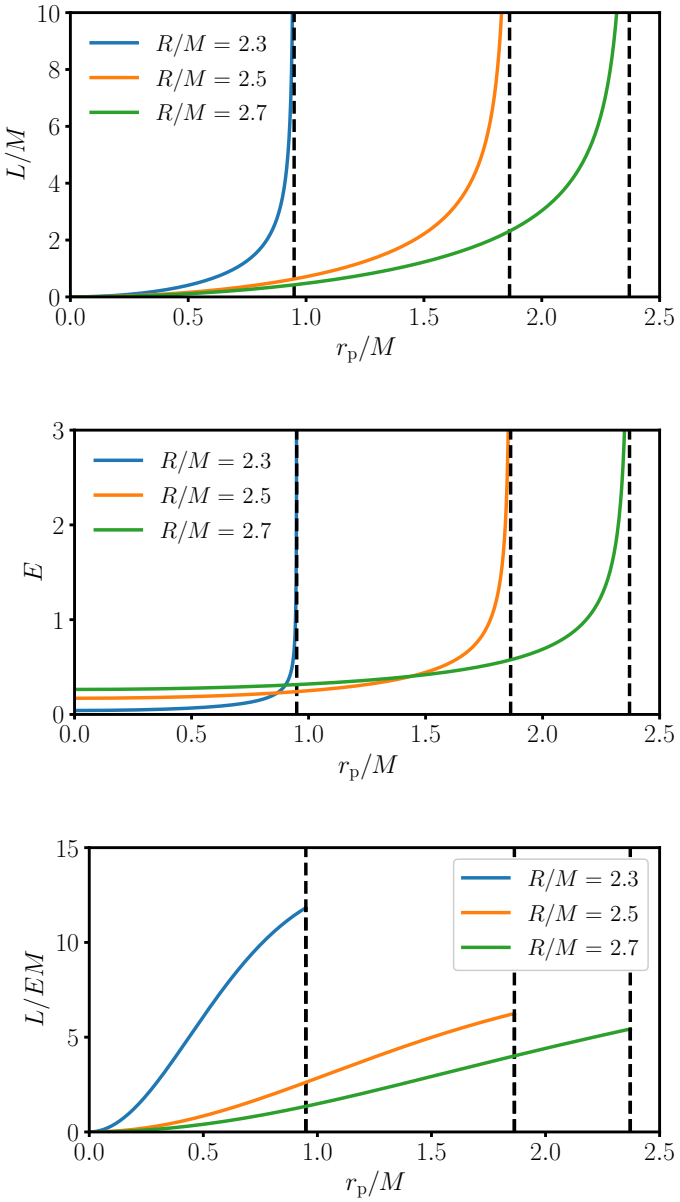

Figure 2.6: Angular momentum (*upper*), energy (*middle*) and their ratio (*lower*) of circular time-like geodesic motions against its radius, for various values of compactness. The dashed lines correspond to those radii of stable light rings, where both L and E diverge and their ratio approaches the light-ring quantity.

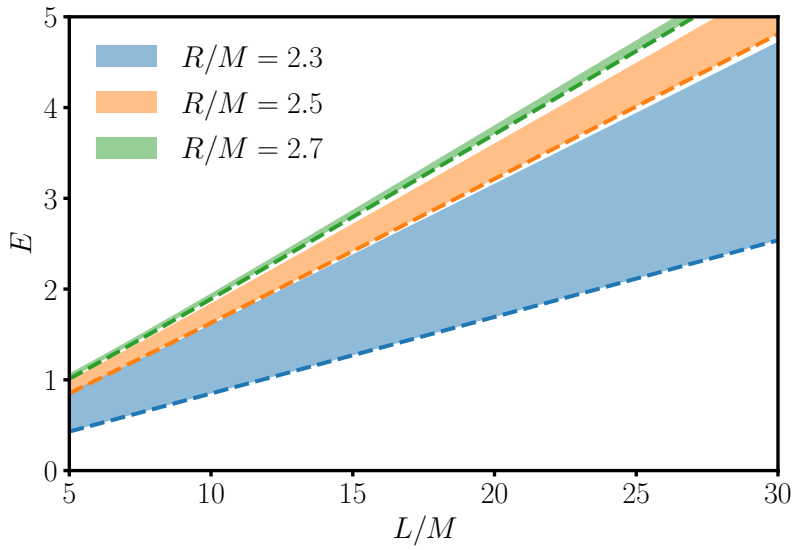

Figure 2.7: The allowed range of energy against angular momentum, with various compactness of stars. The dashed lines correspond to the circular orbits. The allowed range of energy is more narrow for less compact stars, due to the fact that the inside light ring is closer to star surface. The ratio L/E is always smaller than the light-ring impact parameter b_{-}.

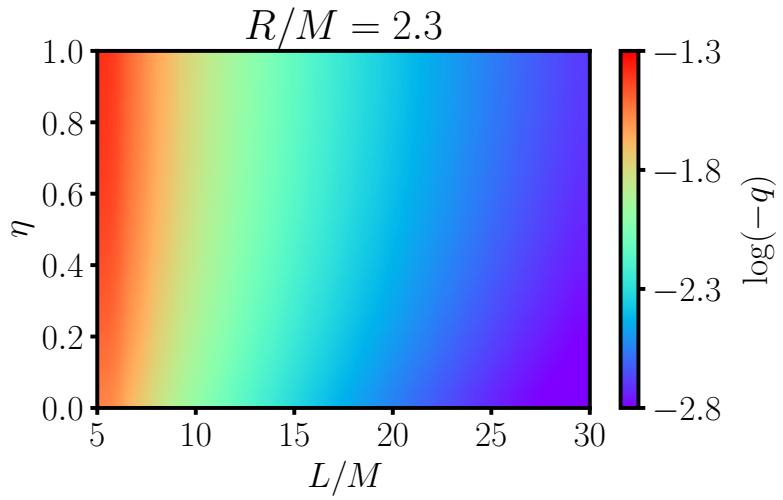

Figure 2.8: The values of q against energy and angular momentum, with $R = 2.3M$ fixed. q varies slowly with energy but rapidly with angular momentum. All values of q are non-zero, implying that the only closed time-like orbits are circular ones. Values of q on the L-axis correspond to circular orbits and thus are supposed to be zero, this feature does not show up in this figure due to the limitation of numerical calculations, while the tendency is clear.

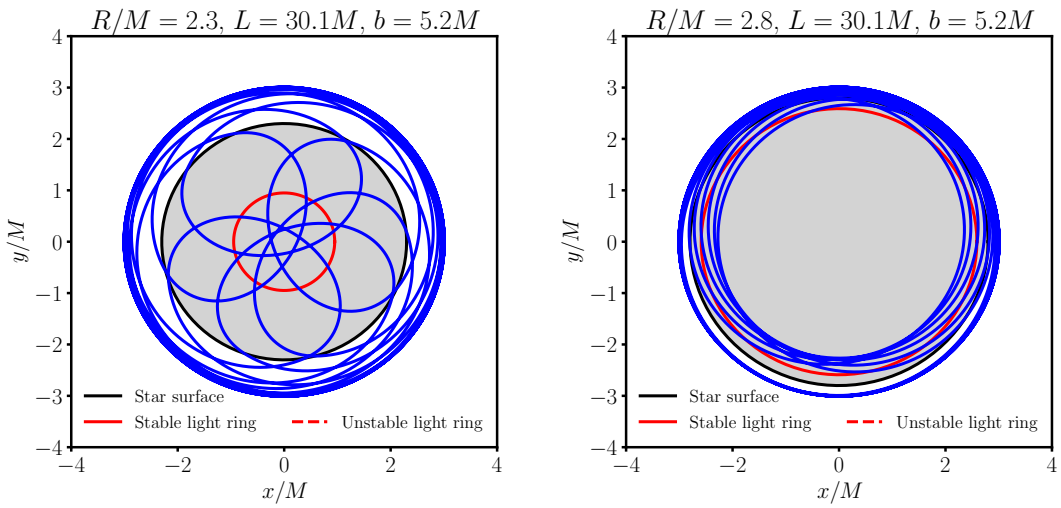

Figure 2.9: Trajectories of time-like particles stably travelling between two light rings. Two orbits share the same energy and angular momentum, while the compactness of star differs. Since the outside spacetimes are the same, the apocenters are identical at $r_{\rm apo} \approx 3.01M$, close to the outside light ring. For the star with $R = 2.3M$, the zoom-whirl behavior is obvious, and its pericenter ($r_{\rm peri} \approx 0.23M \approx 0.24r_{-}$) is far from its inside light ring. For the star with $R = 2.9M$, the orbit is circular-like, and its pericenter ($r_{\rm peri} \approx 2.63M \approx 0.94r_{-}$) is very close to the inside light ring.

Chapter 3

Geodesic synchrotron radiation

Predicted by GR, charged particles orbiting a perturbed Schwarzschild BH near its light ring can emit GSR, regarded an important observational target for early-type gravitational wave telescope. It was shown to be less practical in astrophysics due to the fact that particles are unlikely to stably stay near the unstable light ring. But it can be interesting in the presence of a second, stable light ring inside ECOs since stable particle orbits are allowed near such a light ring.

In this chapter, we study GSR emitted by particles moving in orbits near the stable and unstable light rings of uniform-density stars for scalar, vector (electromagnetic) and tensor (gravitational) cases. For simplicity, we start from scalar radiation by following [76].

3.1 Setup for scalar radiation

Consider a massless scalar field Φ around a compact object of mass M. A point-like particle of mass $m_{\rm p}$ can interact with the scalar field and orbit around the central object. The full dynamics is described by the action

$$S = \int \mathrm{d}^4x\sqrt{-g}\left(\frac{\mathcal{R}}{16\pi} - g^{\mu\nu}\partial_\mu\Phi\partial_\nu\Phi^* - 2q_\Phi\Phi T\right), \tag{3.1}$$

where $g^{\mu\nu}$ is the background metric and $g \equiv \det(g_{\mu\nu})$, $\mathcal{R}$ is the Ricci scalar, $q_\Phi > 0$ is a coupling constant, and T is the trace of the stress tensor of the particle. The point-like particle is considered to be a small perturbation, thus the background spacetime is fixed and taken to be described by a static, spherically symmetric geometry with coordinates $\{t, r, \theta, \phi\}$:

$$\mathrm{d}s^2 = g_{\mu\nu}\mathrm{d}x^\mu\mathrm{d}x^\nu = -f(r)\mathrm{d}t^2 + \frac{1}{g(r)}\mathrm{d}r^2 + r^2(\mathrm{d}\theta^2 + \sin^2\theta\mathrm{d}\phi^2). \tag{3.2}$$

The variation of the action (3.1) yields the scalar field equation of motion coupled to the point-like particle

$$\frac{1}{\sqrt{-g}}\partial_\mu\left(\sqrt{-g}g^{\mu\nu}\partial_\nu\Phi\right)=q_\Phi T. \tag{3.3}$$

We expand the field and the trace in Fourier modes of frequency ω and in spherical harmonics Y_{lm} as

$$\Phi=\sum_{l,m}\int\frac{\mathrm{d}\omega}{\sqrt{2\pi}}e^{-i\omega t}\frac{Z_{lm}(\omega,r)}{r}Y_{lm}(\theta,\phi), \tag{3.4}$$

$$\frac{\sqrt{-g}}{\sin\theta}T=\sum_{l,m}\int\frac{\mathrm{d}\omega}{\sqrt{2\pi}}e^{-i\omega t}T_{lm}Y_{lm}(\theta,\phi), \tag{3.5}$$

where $l\geqslant 0$ and $-l\leqslant m\leqslant l$. By combining Eqs.(3.3), (3.4) and (3.5), we obtain

$$\frac{\mathrm{d}^2Z_{lm}}{\mathrm{d}r_\star^2}+(\omega^2-V)Z_{lm}=S_\Phi, \tag{3.6}$$

where

$$V=l(l+1)\frac{f(r)}{r^2}+\frac{\sqrt{f(r)g(r)}}{r}\left[\sqrt{f(r)g(r)}\right]', \tag{3.7}$$

$$S_\Phi=q_\Phi\frac{\sqrt{f(r)g(r)}}{r}T_{lm}, \tag{3.8}$$

and $r_\star$ denotes the tortoise coordinates, satisfied with $\mathrm{d}r/\mathrm{d}r_\star=\sqrt{f(r)g(r)}$. Here the prime is the derivative with respect to r.

3.2 Source term

In a curved spacetime, the stress tensor describing a free point-like particle is

$$T^{\mu\nu}=\int\frac{m_\mathrm{p}}{\sqrt{-g}}\delta^{(4)}(x-z(\tau))\frac{\mathrm{d}z^\mu}{\mathrm{d}\tau}\frac{\mathrm{d}z^\nu}{\mathrm{d}\tau}\,\mathrm{d}\tau \tag{3.9}$$

$$=\frac{m_\mathrm{p}}{\sqrt{-g}}\frac{\mathrm{d}t_\mathrm{p}}{\mathrm{d}\tau}\frac{\mathrm{d}z^\mu}{\mathrm{d}t}\frac{\mathrm{d}z^\nu}{\mathrm{d}t}\delta(r-r_\mathrm{p})\delta(\theta-\vartheta)\delta(\phi-\varphi), \tag{3.10}$$

where the Dirac δ function in four-dimension is defined as $\int\sqrt{-g}\delta^{(4)}(x)\mathrm{d}^4x=1$ and τ is proper time along the world line $z^\mu=(t_\mathrm{p}(\tau),r_\mathrm{p}(\tau),\vartheta(\tau),\varphi(\tau))$. The trace of this stress tensor is

$$T=g_{\mu\nu}T^{\mu\nu}=-\frac{m_\mathrm{p}}{\sqrt{-g}u_\mathrm{p}^t}\delta(r-R)\delta(\theta-\vartheta)\delta(\phi-\varphi). \tag{3.11}$$

For the equatorial circular motions, we have $\vartheta=\pi/2$ and $\varphi=\Omega_\mathrm{p}t$, where Ω_p is the orbital frequency. By combining Eqs.(3.11) and (3.5), we have

$$-\frac{m_\mathrm{p}}{u_\mathrm{p}^t\sin\theta}\delta(r-r_\mathrm{p})\delta\left(\theta-\frac{\pi}{2}\right)\delta(\phi-\Omega_\mathrm{p}t)=\sum_{l,m}\int\frac{\mathrm{d}\omega'}{\sqrt{2\pi}}e^{-i\omega' t}T_{lm}Y_{lm}(\theta,\phi). \tag{3.12}$$

Multiplying both sides by $Y^*_{l'm'}$ and integrating over sphere, we obtain

$$-\frac{m_{\rm p}}{u^t_{\rm p}}Y^*_{lm}\left(\frac{\pi}{2},0\right)e^{-im\Omega_{\rm p}t}\delta(r-r_{\rm p})=\int\frac{{\rm d}\omega'}{\sqrt{2\pi}}e^{-i\omega' t}T_{lm}, \tag{3.13}$$

where we use the normalization $\int Y_{lm}Y^*_{l'm'}{\rm d}\Omega=\delta_{ll'}\delta_{mm'}$. And multiplying both sides by $e^{i\omega t}$ and integrating in time we get

$$-\int{\rm d}t\frac{m_{\rm p}}{u^t_{\rm p}}Y^*_{lm}\left(\frac{\pi}{2},0\right)e^{-i(m\Omega_{\rm p}-\omega)t}\delta(r-r_{\rm p})=\int{\rm d}t\frac{{\rm d}\omega'}{\sqrt{2\pi}}e^{-i(\omega'-\omega)t}T_{lm}, \tag{3.14}$$

$$-\frac{m_{\rm p}}{u^t_{\rm p}}Y^*_{lm}\left(\frac{\pi}{2},0\right)\delta(m\Omega_{\rm p}-\omega)\delta(r-r_{\rm p})=\int\frac{{\rm d}\omega'}{\sqrt{2\pi}}\delta(\omega'-\omega)T_{lm}, \tag{3.15}$$

$$=\frac{1}{\sqrt{2\pi}}T_{lm}, \tag{3.16}$$

where we use $\delta(x-x_0)=\frac{1}{2\pi}\int e^{it(x-x_0)}{\rm d}t$ and $\int f(x)\delta(x-x_0){\rm d}x=f(x_0)$. Finally, we find

$$T_{lm}=-\sqrt{2\pi}\frac{m_{\rm p}}{u^t_{\rm p}}Y^*_{lm}\left(\frac{\pi}{2},0\right)\delta(m\Omega_{\rm p}-\omega)\delta(r-r_{\rm p}). \tag{3.17}$$

3.3 Energy flux

With the source term, we are now able to solve the differential equation (3.6). We temporarily omit the indexes lm, and consider $Z_{\rm in}$ and $Z_{\rm out}$ are two linearly independent solutions to the homogeneous equation

$$\frac{{\rm d}^2Z}{{\rm d}r^2_\star}+(\omega^2-V)Z=0. \tag{3.18}$$

We impose that $Z_{\rm in}$ is a solution regular at an inner boundary at $r=r_{\rm in}$ and $Z_{\rm out}$ is a solution regular at an outer boundary at $r=r_{\rm out}$. Since we are interested in the radiation that escapes to infinity, we need to study the behaviour of the solution to Eq.(3.18) far from the central object. At infinity, the homogeneous equation reduces to

$$\frac{{\rm d}^2Z}{{\rm d}r^2_\star}+\omega^2Z=0, \tag{3.19}$$

which has the general solution $c_1e^{i\omega r_\star}+c_2e^{-i\omega r_\star}$. Thus, we can impose the boundary condition at infinity:

$$Z_{\rm in}(r_\star\to+\infty)=A_{\rm in}e^{-i\omega r_\star}+A_{\rm out}e^{i\omega r_\star}, \tag{3.20}$$

$$Z_{\rm out}(r_\star\to+\infty)=e^{i\omega r_\star}. \tag{3.21}$$

And the Wronskian can be found at infinity as

$$W(Z_{\rm in},Z_{\rm out})=Z_{\rm in}\frac{{\rm d}Z_{\rm out}}{{\rm d}r_\star}-Z_{\rm out}\frac{{\rm d}Z_{\rm in}}{{\rm d}r_\star}=2i\omega A_{\rm in}. \tag{3.22}$$

For the source term presented in $r_\star^{\rm in} < r_\star < r_\star^{\rm out}$, we have the formal solution to Eq.(3.6) as

$$Z(r_\star) = Z_{\rm out}\int_{r_\star^{\rm in}}^{r_\star}\frac{S_\Phi Z_{\rm in}}{W(Z_{\rm in},Z_{\rm out})}\,{\rm d}r'_\star + Z_{\rm in}\int_{r_\star}^{r_\star^{\rm out}}\frac{S_\Phi Z_{\rm out}}{W(Z_{\rm in},Z_{\rm out})}\,{\rm d}r'_\star, \tag{3.23}$$

where the Wronskian $W(Z_{\rm in},Z_{\rm out})$ is a constant due to the form of Eq.(3.6).

As the second term in the right hand side of Eq.(3.23) vanishes at infinity, we have the behavior of solution (3.23) far from the object as

$$\begin{aligned} Z(r_\star\to+\infty) &= Z_{\rm out}\int_{r_\star^{\rm in}}^{r_\star}\frac{S_\Phi Z_{\rm in}}{W(Z_{\rm in},Z_{\rm out})}\,{\rm d}r'_\star & (3.24)\\ &= -\frac{e^{i\omega r_\star}}{2i\omega A_{\rm in}}\sqrt{2\pi}q_\Phi m_{\rm p}Y^*_{lm}\left(\frac{\pi}{2},0\right)\frac{Z_{\rm in}(r_{\rm p})}{r_{\rm p}u^r(r_{\rm p})}\delta(m\Omega_{\rm p}-\omega) & (3.25)\\ &= e^{i\omega r_\star}Z^\infty_{lm}\delta(m\Omega_{\rm p}-\omega), & (3.26)\end{aligned}$$

where we define

$$Z^\infty_{lm} = -\frac{1}{2i\omega A_{\rm in}}\sqrt{2\pi}q_\Phi m_{\rm p}Y^*_{lm}\left(\frac{\pi}{2},0\right)\frac{Z_{\rm in}(r_{\rm p})}{r_{\rm p}u^t_{\rm p}}. \tag{3.27}$$

The energy flux emitted by the scalar field at infinity is

$$\dot{E} = \frac{{\rm d}E}{{\rm d}t} = \lim_{r\to\infty}\int{\rm d}\theta{\rm d}\phi\sqrt{-g}T^{(\Phi)}_{rt}, \tag{3.28}$$

where $T^{(\Phi)}_{rt}$ is the relevant component of the stress tensor of the scalar field

$$T^{(\Phi)}_{\mu\nu} = \partial_\mu\Phi\partial_\nu\Phi^* - \frac{1}{2}g_{\mu\nu}\partial_a\Phi\partial^a\Phi^*. \tag{3.29}$$

Inserting the spherical harmonics expansion (3.4) and the asymptotic behaviour at large distance

$$Z_{lm}\sim e^{i\omega r}Z^\infty_{lm}\delta(m\Omega_{\rm p}-\omega), \tag{3.30}$$

we find

$$\frac{{\rm d}^2E}{{\rm d}t{\rm d}\Omega} = \frac{1}{2\pi}\sum_{l,m}\sum_{l',m'}\int{\rm d}\omega{\rm d}\omega' Y_{lm}Y^*_{l'm'}e^{i(\omega-\omega')(r-t)}Z^\infty_{lm}Z^\infty_{l'm'}\delta(m\Omega_{\rm p}-\omega)\delta(m'\Omega'_{\rm p}-\omega'). \tag{3.31}$$

Taking the normalization condition $\int{\rm d}\Omega Y_{lm}Y^*_{l'm'} = \delta_{ll'}\delta_{mm'}$, the above expression reduces to

$$\dot{E}_{lm} = \frac{1}{2\pi}(m\Omega_{\rm p})^2\left|Z^\infty_{lm}\right|^2, \tag{3.32}$$

and the total flux $\dot{E}$ is given by the sum of $\dot{E}_{lm}$ over l and m.

3.4 Schwarzschild black hole case

In the case of Schwarzschild BH, we have $f(r) = g(r) = 1 - \frac{2M}{r}$, and thus

$$V_{\rm Sch} = \left(1 - \frac{2M}{r}\right)\left[\frac{l(l+1)}{r^2} + \frac{2M}{r^3}\right], \tag{3.33}$$

$$r_\star = \int \left(\frac{{\rm d}r_\star}{{\rm d}r}\right) {\rm d}r = r + 2M \ln\left(\frac{r}{M} - 2\right). \tag{3.34}$$

At the horizon $r \to r_{\rm H} \equiv 2M$, we have $V_{\rm Sch} \to 0$ and $r_\star \to -\infty$, which means the homogeneous equation (3.18) also reduces to Eq.(3.19). Thus we can impose the boundary condition at the horizon:

$$Z_{\rm in}(r_\star \to -\infty) = e^{i\omega r_\star}, \tag{3.35}$$

$$Z_{\rm out}(r_\star \to -\infty) = B_{\rm in} e^{-i\omega r_\star} + B_{\rm out} e^{i\omega r_\star}. \tag{3.36}$$

With this boundary condition, we are able to numerically solve $Z_{\rm in}(r_{\rm p})$ and $A_{\rm in}$, allowing us to compute the energy flux at infinity.

Moreover, in the low frequency limit $\omega r_{\rm H} \ll 1$, [77] find

$$\dot{E} \approx \frac{m_{\rm p}^2 q_\Phi^2}{4\pi} \frac{\omega^{2l+2} r_{\rm p}^{2l}}{\Gamma(2l+2)} = \frac{m_{\rm p}^2 q_\Phi^2}{4\pi} \frac{l^{2l+2} M^{l+1}}{r_{\rm p}^{l+3} \Gamma(2l+2)}, \tag{3.37}$$

which requires

$$l \ll \frac{1}{2}\left(\frac{r_{\rm p}}{M}\right)^{\frac{3}{2}}. \tag{3.38}$$

Figure 3.1 displays the numerical results of the energy flux given by Eq.(3.32) together with the low-frequency limit for particles orbiting around a Schwarzschild BH at $r_{\rm p} = 10M$ and $25M$, where we define $\dot{\mathcal{E}} = \dot{E}_{lm}/(m_{\rm p}^2 q_\Phi^2)$. We find the energy radiation is dominated by low frequency modes when a particle is far from the unstable light ring. The agreement between the numerical results and the low-frequency limit is better for less energetic orbits which are farther from the BH.

For particles located in those most inwardly reachable orbits, [57] find the radiation is dominated by higher-frequency modes, rather than low-frequency modes, and over 99.9% of the power is radiated in $l = m$ modes. An approximate expression for energy flux reads [57]

$$\dot{E}_m = \frac{m_{\rm p}^2 q_\Phi^2}{27\pi^{\frac{5}{2}} M^2} \frac{m}{m_{\rm crit}} e^{-\frac{\pi\epsilon}{4}} \Gamma^2\left(\frac{1+i\epsilon}{4}\right), \tag{3.39}$$

where

$$\epsilon = 1 + \frac{4}{\pi}\frac{m}{m_{\rm crit}}, \tag{3.40}$$

$$m_{\rm crit} = \frac{4}{\pi\delta}. \tag{3.41}$$

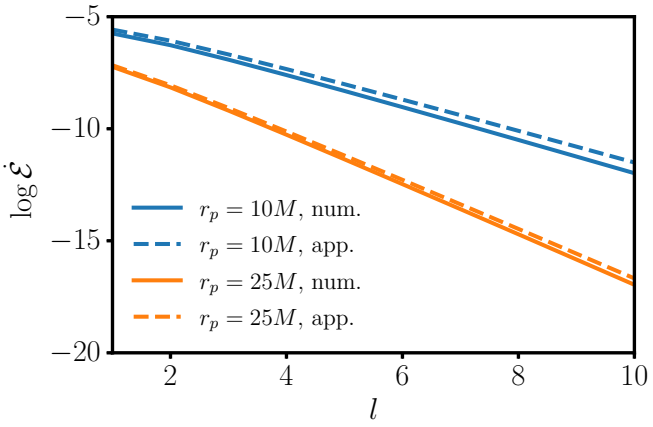

Figure 3.1: Scalar energy fluxes at infinity as a function of l in logarithmic scale, for the Schwarzschild BH case with particles orbiting at $r_{\rm p} = 10M$ (in blue) and $25M$ (in orange). The solid lines correspond to numerical results and the dashed lines correspond to approximation results. It is intuitive in this figure that the approximation expression approximates the numerical results better at larger particle orbiting radii.

Figure 3.2 shows the numerical results of (3.32) together with the high-frequency limit given by Eq.(3.39), where their agreement is better for less energetic orbits which are farther from the BH. It turns out the radiation reaches its peak at $m \approx m_{\rm crit} \gg 1$, and the total power is found numerically as $\dot{E} \propto m_{\rm p}^2 q_\Phi^2/(M^2\delta)$, diverging at the unstable light ring.

3.5 Uniform-density star case

In the case of uniform-density star, $f(r)$ and $g(r)$ are piecewise functions: for $r < R$, $f(r) = g(r) = 1 - (2M/r)$ and for $r > R$, $f(r)$ and $g(r)$ are given by Eqs.(2.2) and (2.3) respectively. The expression of $r_\star$ is thus more complicated:

$$r_\star = \begin{cases} r + 2M \ln\left(\dfrac{r}{M} - 2\right) + r_R, & r > R, \\ \dfrac{R^2 y_1 y_3 (3Ry_1 - y_3)\left[\arctan\left(\frac{r\sqrt{M}}{Ry_2}\right) + \arctan\left(\frac{3ry_1\sqrt{M}}{y_2 y_3}\right)\right]}{y_1 y_2 y_3 \sqrt{-2M\left[3Ry_1 y_3 + M(r^2 + 9R^2) - 5R^3\right]}}, & r < R, \end{cases} \tag{3.42}$$

where

$$y_1 = \sqrt{R - 2M}, \tag{3.43}$$
$$y_2 = \sqrt{4R - 9M}, \tag{3.44}$$
$$y_3 = \sqrt{R^3 - 2Mr^2}, \tag{3.45}$$

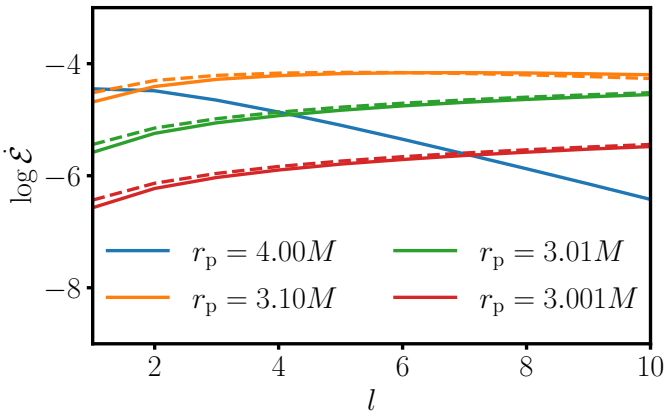

Figure 3.2: Scalar energy radiation as a function of l, for the Schwarzschild BH case, with particles orbiting at $r_{\rm p} \gtrsim r_+$. The solid lines correspond to numerical results and the dashed lines correspond to approximation results. When particles' orbits are close enough to the unstable light ring, the radiation is dominated by higher-frequency modes, leading to the divergence of total energy flux.

and r_R is a properly chosen integral constant to ensure $r_\star(r)$ is continuous at star surface $r = R$.

Near the center of the star, the homogeneous equation (3.18) reduces to

$$\frac{\mathrm{d}^2 Z}{\mathrm{d}r^2} - \frac{l(l+1)}{r^2} Z = 0, \tag{3.46}$$

which has the general solution $c_3 r^{l+1} + c_4/r^l$. Hence we impose the boundary condition at the center:

$$Z_{\rm in}(r \to 0) = r^{l+1}, \tag{3.47}$$

$$Z_{\rm out}(r \to 0) = C r^{l+1} + \frac{D}{r^l}. \tag{3.48}$$

Also, we impose the continuous condition that $Z_{\rm in}$, $Z_{\rm out}$, and their derivatives, $\mathrm{d}Z_{\rm in}/\mathrm{d}r$, $\mathrm{d}Z_{\rm out}/\mathrm{d}r$, are continuous at the star surface.

The energy flux at infinity can be obtained numerically. In Figure 3.3, we display scalar energy flux emitted by particles orbiting around a uniform-density star near its unstable light ring, with $R = 2.3M$ and $R = 2.9M$. For the more compact star ($R = 2.3M$), we see peaks and valleys due to trapped modes described in [34, 70, 78] (and [79] for a review). Apart from the excitations, the flux is almost the same as that in the case of a Schwarzschild BH, and higher frequency modes contributes more as particles get close to the unstable light ring. For the less compact star ($R = 2.9M$), we find no excited mode since trapped modes only appear in higher-l modes, and the flux is close to that in Schwarzschild BH case.

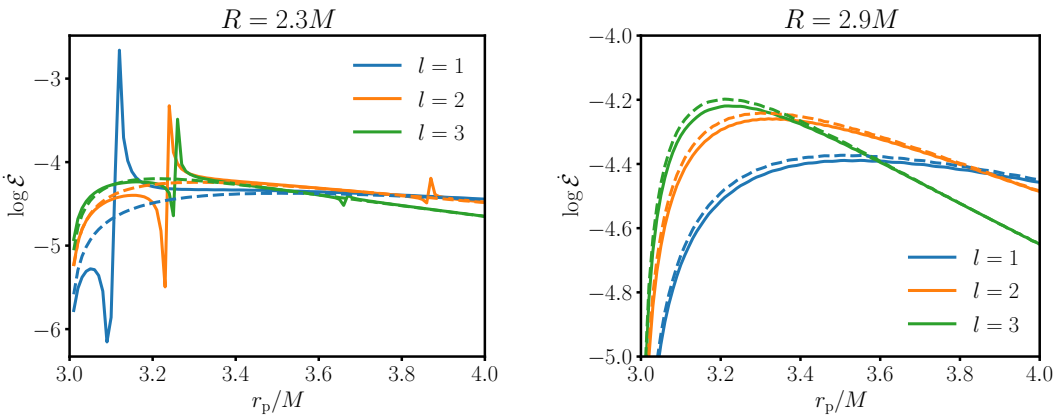

Figure 3.3: Scalar energy flux emitted by particles orbiting a uniform-density star near its unstable light ring at $r_+ = 3M$, with $R = 2.3M$ (*left*) and $R = 2.9M$ (*right*), shown in solid lines. Dashed lines show the energy flux emitted by particles orbiting a Schwarzschild BH. In the left panel, we see peaks and valleys due to the trapped modes due to the potential barrier inside the star. Apart from the excitations, the radiation is almost the same as that in Schwarzschild BH case: as particles get close to the unstable light ring, the higher frequency modes contribute more.

Table 3.1: Trapped modes of scalar radiation in $R = 2.3M$ uniform-density star case, given by the WKB approximation following [34], together with corresponding particle's orbital radii. These radii are located close to the positions of excitation shown in Figure 3.3. For $l = 1$, the trapped-mode radius does not well agree with the excitation radius due to the WKB approximation breaks down for smaller l. A more robust method for trapped modes is described in [80].

	$n = 0$	$n = 1$	$n = 2$
$l = 1$	$\Omega_{\rm p} M = 0.1758$ $r_{\rm p}/M = 3.18$		
$l = 2$	$\Omega_{\rm p} M = 0.2592$ $r_{\rm p}/M = 3.90$	$\Omega_{\rm p} M = 0.3396$ $r_{\rm p}/M = 3.26$	
$l = 3$		$\Omega_{\rm p} M = 0.4250$ $r_{\rm p}/M = 3.68$	$\Omega_{\rm p} M = 0.5076$ $r_{\rm p}/M = 3.27$

In Figure 3.4, we present scalar energy flux emitted by particles orbiting a uniform-density star near its stable light ring. We observe that the radiation is suppressed near the light ring in both $R = 2.3M$ and $R = 2.9M$ cases. In the $R = 2.3M$ case, we find $l = |m| = 1$ mode contributes most energy flux. This differs from the flux emitted from the unstable light ring. Also, there is no resonant configuration as the frequencies are away from those resonant ones shown in Table 3.1.

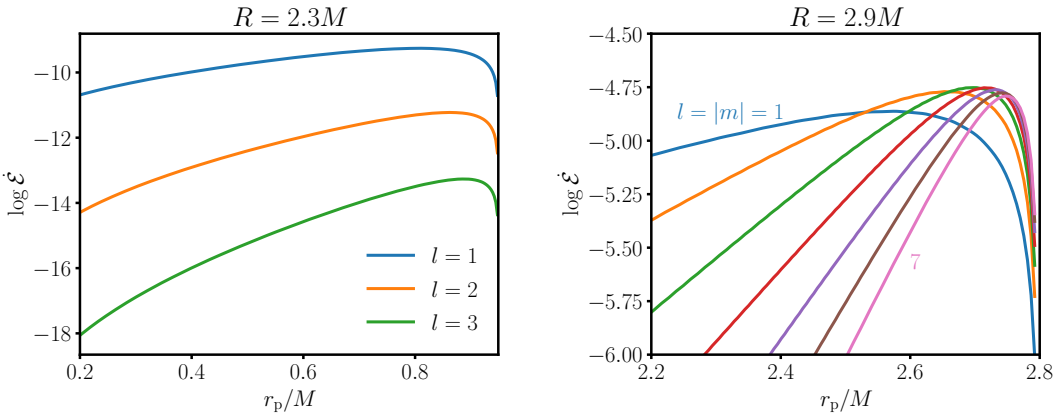

Figure 3.4: Scalar energy flux emitted by particles orbiting a uniform-density star near its stable light ring, with $R = 2.3M$ (*left*) and $R = 2.9M$ (*right*). In the $R = 2.3M$ case, $l = 1$ mode contributes the flux dominantly and the flux is also depressed near the stable light ring. In the $R = 2.9M$ case, we find higher frequency modes contribute more.

To understand what causes the radiation suppression near the stable light ring, we look into the analytical expression of energy flux emitted by particles orbiting near r_-. For $l \gg 1$ modes, the potential $V(r)$ reduces to

$$V(r) \simeq l(l+1)\frac{f(r)}{r^2} = l(l+1)V_{\rm null}(r). \tag{3.49}$$

We have found that $V_{\rm null}(r)$ reaches its local minimum at the stable light ring, and thus $2f(r_-) - r_- f'(r_-) = 0$. The local minimum of $V(r)$ is given by $l(l+1)\frac{f(r_-)}{r^2} = l(l+1)\frac{f'(r_-)}{2r_-} = l(l+1)\Omega_{\rm p}^2(r_-)$. As $\Omega_{\rm p}(r) < \Omega_{\rm p}(r_-)$, we have that $V(r) > \omega^2$ always holds valid inside the star. Only one turning point $r_\star^0$ exists outside the star, satisfying that $V(r_\star^0) = \omega^2$, as shown in Figure 3.5.

The standard WKB approximation method gives us the general solution to Eq.(3.18):

$$\psi(r_\star) = \begin{cases} \dfrac{1}{\sqrt{|p(r_\star)|}}\left[De^{\int_{r_\star}^{r_\star^0}|p(r'_\star)|{\rm d}r'_\star} + Fe^{-\int_{r_\star}^{r_\star^0}|p(r'_\star)|{\rm d}r'_\star}\right], & r_\star < r_\star^0, \\ \dfrac{1}{\sqrt{p(r_\star)}}\left[Be^{i\int_{r_\star^0}^{r_\star} p(r'_\star){\rm d}r'_\star} + Ce^{-i\int_{r_\star^0}^{r_\star} p(r'_\star){\rm d}r'_\star}\right], & r_\star > r_\star^0, \end{cases} \tag{3.50}$$

where

$$p(r_\star) \equiv \sqrt{\omega^2 - V(r_\star)}. \tag{3.51}$$

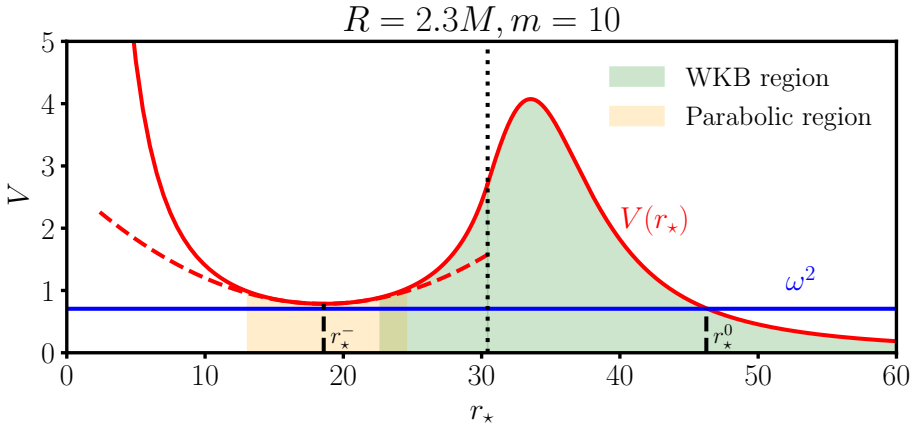

Figure 3.5: $V(r)$ (red solid curve) and Ω^2 (blue solid line) in the differential equation (3.18), for the case of $R = 2.3M$ and $l = m = 10$. The black dotted line corresponds the star surface, and the black dashed lines correspond to the inner light ring at $r_\star^-$ and the turning point $r_\star^0$. The WKB region and parabolic region are respectively shown in green and orange shaded regions. In the overlap region, both approximations hold valid. The red dashed curve shows the parabolic potential.

The relation of coefficients can be obtained by using a linear patching function to connect two sides, which is

$$D = Be^{-i\frac{\pi}{4}} + Ce^{i\frac{\pi}{4}}, \tag{3.52}$$

$$F = \frac{1}{2}Be^{i\frac{\pi}{4}} + \frac{1}{2}Ce^{-i\frac{\pi}{4}}. \tag{3.53}$$

As we are interested in the solution $Z_{\rm in}(r_{\rm p} \approx r_-)$, where WKB approximation breaks down, we apply the parabolic approximation near the stable light ring at $r_\star^-$. We assume that $V(r_\star)$ can be approximately expressed as a parabolic function near $r_\star^-$, and in the region where parabolic approximation holds, we have

$$V(r_\star) \simeq \omega^2 + \frac{1}{2}\left.\frac{\mathrm{d}^2V}{\mathrm{d}r_\star^2}\right|_{r_\star=r_\star^-}(r_\star - r_\star^-)^2 + \Delta. \tag{3.54}$$

By defining

$$\beta^4 = \frac{1}{2}\left.\frac{\mathrm{d}^2V}{\mathrm{d}r_\star^2}\right|_{r_\star=r_\star^-}, \tag{3.55}$$

$$x = \beta(r_\star - r_\star^-), \tag{3.56}$$

$$\Delta = V(r_\star^-) - \omega^2, \tag{3.57}$$

$$\epsilon = \frac{\Delta}{\beta^2}, \tag{3.58}$$

Eq.(3.18) becomes

$$\frac{\mathrm{d}^2Z}{\mathrm{d}x^2} - (x^2 - \epsilon)Z = 0. \tag{3.59}$$

Its general solution is given by

$$Z(x) = \mathcal{A} \cdot D_{-\frac{1}{2}-\frac{\epsilon}{2}}(\sqrt{2}x) + \mathcal{B} \cdot D_{-\frac{1}{2}-\frac{\epsilon}{2}}(-\sqrt{2}x), \tag{3.60}$$

where $D_{-\frac{1}{2}-\frac{\epsilon}{2}}(\pm\sqrt{2}x)$ are parabolic cylinder functions. $D_{-\frac{1}{2}-\frac{\epsilon}{2}}(\pm\sqrt{2}x)$ are linear independent only if $-\frac{1}{2}-\frac{\epsilon}{2}$ is non-integer. However, only very particular R and $r_{\rm p}$ makes $-\frac{1}{2}-\frac{\epsilon}{2}$ an integer. At least in most cases, it is safe to assume $-\frac{1}{2}-\frac{\epsilon}{2}$ is non-integer. To connect the solution to the WKB solution, we assume that there exists a overlap region where both the WKB approximation and the parabolic approximation hold simultaneously, and such a region is located far from $r_\star^-$, i.e. $x \gg 0$. The general solution (3.60) has the asymptotic behavior at $x \gg 0$ as

$$Z(x \gg 0) \simeq \left(\mathcal{A} - i\mathcal{B}e^{-i\frac{\pi}{2}\epsilon}\right) 2^{-\frac{1}{4}-\frac{\epsilon}{4}} e^{-\frac{x^2}{2}} x^{-\frac{1}{2}-\frac{\epsilon}{2}} + \mathcal{B}\frac{\sqrt{\pi}2^{\frac{1}{4}+\frac{\epsilon}{4}}}{\Gamma\left(\frac{1+\epsilon}{2}\right)} e^{\frac{x^2}{2}} x^{-\frac{1}{2}+\frac{\epsilon}{2}}. \tag{3.61}$$

Now we are able to explicitly obtain the WKB solution at the overlap region. Since we have

$$\begin{aligned}
|p(r_\star)| &\simeq \sqrt{\left|\omega^2 - \left[\omega^2 + \beta^4(r_\star - r_\star^-)^2 + \Delta\right]\right|} && (3.62)\\
&= \sqrt{\beta^4(r_\star - r_\star^-)^2 + \Delta} && (3.63)\\
&\approx \beta^2(r_\star - r_\star^-), && (3.64)\\
\int_{r_\star}^{r_\star^-} |p(r'_\star)|\,\mathrm{d}r'_\star &= \int_{r_\star}^{r_\star^-} \sqrt{\beta^4(r_\star - r_\star^-)^2 + \Delta}\,\mathrm{d}r'_\star && (3.65)\\
&= \frac{\Delta\ln(\beta^2\sqrt{\Delta})}{2\beta^2} - \frac{1}{2}(r_\star - r_\star^-)\sqrt{\beta^4(r_\star - r_\star^-)^2 + \Delta} && (3.66)\\
&\quad -\frac{\Delta}{2\beta^2}\ln\left[\beta^4(r_\star - r_\star^-) + \beta^2\sqrt{\beta^4(r_\star - r_\star^-)^2 + \Delta}\right] && (3.67)\\
&\approx \frac{\Delta\ln(\beta^2\sqrt{\Delta})}{2\beta^2} - \frac{1}{2}\beta^2(r_\star - r_\star^-)^2 - \frac{\Delta}{2\beta^2}\ln\left[2\beta^4(r_\star - r_\star^-)\right], && (3.68)
\end{aligned}$$

the WKB solution (3.50) in $r_\star < r_\star^0$ can be written as

$$\begin{aligned}
Z(r_\star) &= \frac{1}{\sqrt{|p(r_\star)|}}\left[De^{\kappa}e^{\int_{r_\star}^{r_\star^-}|p(r'_\star)|\mathrm{d}r'_\star} + Fe^{-\kappa}e^{-\int_{r_\star}^{r_\star^-}|p(r'_\star)|\mathrm{d}r'_\star}\right], && (3.69)\\
&= De^{\kappa}2^{-\frac{\epsilon}{2}}\beta^{-\frac{1}{2}-\frac{\epsilon}{2}}e^{-\frac{x^2}{2}}x^{-\frac{1}{2}-\frac{\epsilon}{2}} + Fe^{-\kappa}2^{\frac{\epsilon}{2}}\beta^{-\frac{1}{2}+\frac{\epsilon}{2}}e^{\frac{x^2}{2}}x^{-\frac{1}{2}+\frac{\epsilon}{2}}, && (3.70)
\end{aligned}$$

where

$$\kappa \equiv \int_{r_\star^-}^{r_\star^0} |p(r'_\star)|\,\mathrm{d}r'_\star. \tag{3.71}$$

By comparing (3.61) and (3.70), we obtain

$$\begin{aligned}
\left(\mathcal{A} - i\mathcal{B}e^{-i\frac{\pi}{2}\epsilon}\right) &= De^{\tau}2^{\frac{1}{4}-\frac{\epsilon}{4}}\beta^{-\frac{1}{2}-\frac{\epsilon}{2}}, && (3.72)\\
\mathcal{B} &= Fe^{-\tau}2^{-\frac{1}{4}+\frac{\epsilon}{4}}\beta^{-\frac{1}{2}+\frac{\epsilon}{2}}\frac{\Gamma\left(\frac{1+\epsilon}{2}\right)}{\sqrt{\pi}}. && (3.73)
\end{aligned}$$

Now let us consider the boundary condition for $Z_{\rm in}$:

$$Z_{\rm in}(r_\star) = \begin{cases} r^{l+1}, & r \to 0, \\ A_{\rm in}e^{-i\omega r_\star} + A_{\rm out}e^{i\omega r_\star}, & r_\star \to +\infty. \end{cases} \tag{3.74}$$

At infinity, we find

$$A_{\rm in} = \frac{C}{\sqrt{\omega}}, \tag{3.75}$$

$$A_{\rm out} = \frac{B}{\sqrt{\omega}}. \tag{3.76}$$

However, parabolic approximation breaks down at $r \to 0$ ($r_\star \to 0$), we cannot connect $Z_{\rm in} = r^{l+1}$ to the solution. Numerical solution shows that $Z_{\rm in}$ monotonically increases inside the star, namely it decreases from surface to center. Therefore, we demand $D = 0$. Otherwise the solution increases exponentially from surface to center. It leads to

$$B = -iC, \tag{3.77}$$

$$F = Ce^{-i\frac{\pi}{4}}, \tag{3.78}$$

$$\mathcal{A} = i\mathcal{B}e^{-i\frac{\pi}{2}\epsilon}, \tag{3.79}$$

$$\mathcal{B} = e^{-i\frac{\pi}{4}}\sqrt{\omega}A_{\rm in}e^{-\kappa}2^{-\frac{1}{4}+\frac{\epsilon}{4}}\beta^{-\frac{1}{2}+\frac{\epsilon}{2}}\frac{\Gamma\left(\frac{1+\epsilon}{2}\right)}{\sqrt{\pi}}., \tag{3.80}$$

and thus near the inner light ring, we have

$$Z_{\rm in}(x=0) = (\mathcal{A}+\mathcal{B})\, D_{-\frac{1}{2}-\frac{\epsilon}{2}}(0) \tag{3.81}$$

$$= \left(1 + ie^{-i\frac{\pi}{2}\epsilon}\right)\mathcal{B}\cdot D_{-\frac{1}{2}-\frac{\epsilon}{2}}(0) \tag{3.82}$$

$$= \left(1 + ie^{-i\frac{\pi}{2}\epsilon}\right)e^{-i\frac{\pi}{4}}\frac{\sqrt{\omega}A_{\rm in}}{\sqrt{2}}e^{-\kappa}\beta^{-\frac{1}{2}+\frac{\epsilon}{2}}\frac{\Gamma\left(\frac{1+\epsilon}{2}\right)}{\Gamma\left(\frac{3}{4}+\frac{\epsilon}{4}\right)} \tag{3.83}$$

$$= \left(1 + ie^{-i\frac{\pi}{2}\epsilon}\right)e^{-i\frac{\pi}{4}}\frac{\sqrt{\omega}A_{\rm in}}{\sqrt{\pi}}e^{-\kappa}\beta^{-\frac{1}{2}+\frac{\epsilon}{2}}2^{\frac{\epsilon}{2}-1}\Gamma\left(\frac{1}{4}+\frac{\epsilon}{4}\right). \tag{3.84}$$

The energy radiation for $l \gg 1$ mode is

$$\dot{E}_{lm} = \frac{1}{2\pi}(m\Omega)^2\cdot\frac{1}{4\omega^2A_{\rm in}^2}2\pi q_\Phi^2 m_{\rm p}^2 Y_{lm}^2\left(\frac{\pi}{2},0\right)\frac{Z_{\rm in}^2(x=0)}{r_{\rm p}^2\left[u^t(r_{\rm p})\right]^2} \tag{3.85}$$

$$= \frac{q_\Phi^2 m_{\rm p}^2}{r_{\rm p}^2\left[u^t(r_{\rm p})\right]^2}\frac{m\omega_0 Y_{lm}^2\left(\frac{\pi}{2},0\right)}{\pi}\left(1+\sin\frac{\epsilon\pi}{2}\right)e^{-2\kappa}\beta^{\epsilon-1}2^{\epsilon-3}\Gamma^2\left(\frac{1+\epsilon}{4}\right). \tag{3.86}$$

The comparison between numerical results of scalar radiation and the analytical ones obtained from Eq. (3.86) is displayed in Figure 3.6. For any given indices lm, we find $\dot{E}_{lm} \to 0$ at $r_{\rm p} \to r_-$ due to the fact that $u_{\rm p}^t$ diverges. At a fix $r_{\rm p}$, most radiation is contributed from $l = |m|$ modes since the barrier factor κ is larger for $l > |m|$ modes. We can actually see these features near both stable and unstable light ring. However, since κ increases proportionally with l in $l = |m|$ modes, higher l modes are thus suppressed, the radiation is dominated by lower l modes. This suppression is less obvious for less compact stars, due to the potential barrier is lower thus κ increases too slow with l.

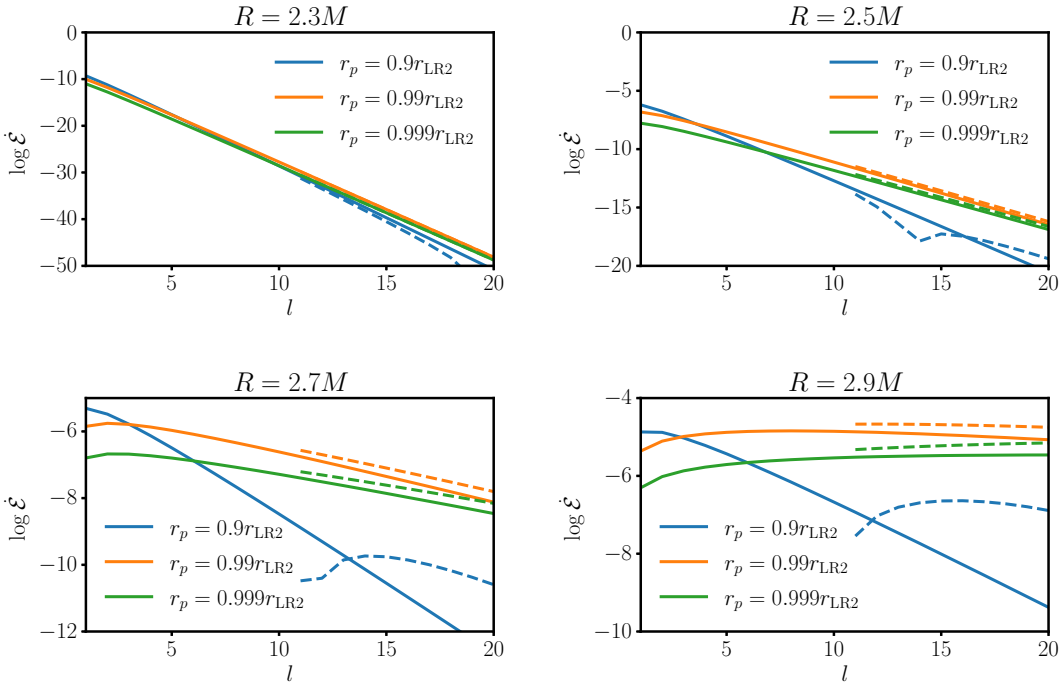

Figure 3.6: Scalar fluxes of particles orbiting inside the stable light ring of uniform-density stars, for various star compactness and orbiting radii. The analytical expression (3.86) approximates numerical results better when closer to the light ring and for more compact stars.

3.6 Electromagnetic and gravitational radiation

Following a similar strategy as in the scalar case, it is in principle viable to obtain equations describing electromagnetic or gravitational perturbation produced by an electric charged or massive point source, by expanding the perturbations into angular harmonics [81–86]. The details are not part of this thesis, but will be included in a paper to be published.

The electromagnetic perturbations are described by

$$\frac{\mathrm{d}^2 Z_{\mathrm{a,p}}}{\mathrm{d}r_\star^2} + (\omega^2 - V_{\mathrm{EM}}) Z_{\mathrm{a,p}} = S_{\mathrm{a,p}}, \tag{3.87}$$

where the index corresponds to axial (a) and polar (p) perturbations and

$$V_{\mathrm{EM}} = l(l+1)\frac{f(r)}{r^2}. \tag{3.88}$$

For circular motions, the source terms are given by

$$S_{\mathrm{a}} = \frac{4\pi f(r)\Omega_{\mathrm{p}}}{l(l+1)} \frac{\partial Y^*_{lm}\left(\frac{\pi}{2}, 0\right)}{\partial\theta} \delta(r - r_{\mathrm{p}}), \tag{3.89}$$

$$S_{\mathrm{p}} = \frac{i4\pi m q_{\mathrm{E}} \sqrt{f(r)g(r)}\Omega_{\mathrm{p}}}{l(l+1)} Y^*_{lm}\left(\frac{\pi}{2}, 0\right) \frac{\mathrm{d}}{\mathrm{d}r}\left[f(r)\delta(r - r_{\mathrm{p}})\right], \tag{3.90}$$

where q_{E} is electric charged carried by the particle. And the energy fluxes are computed from

$$\dot{E}_{\mathrm{a,p}} = \frac{l(l+1)}{2\pi} |Z_{\mathrm{a,p}}|^2. \tag{3.91}$$

Numerical results are presented in Figure 3.7 for axial radiation and in Figure 3.8 for polar radiation. Differing from the scalar case, electromagnetic radiation converge to a certain value near light rings. Axial electromagnetic radiation is dominated by lower l modes. Negligible excitations are found in axial radiation emitted by particles orbiting near the unstable light ring. Though the negligibility is possible due to the lack of resolution, axial excitations are at least much less significant than polar excitations. At any fixed l, polar radiation is significantly larger than axial radiation, except for those obvious excitation from particles orbiting near the unstable light ring.

The axial gravitational perturbations are described by

$$\frac{\mathrm{d}^2 Z_{\mathrm{g}}}{\mathrm{d}r_\star^2} + (\omega^2 - V_{\mathrm{g}}) Z_{\mathrm{g}} = S_{\mathrm{g}}, \tag{3.92}$$

where

$$V_{\mathrm{g}} = f(r)\left[\frac{l(l+1)}{r^2} + \frac{3g(r) - 3}{r^2} + 4\pi(\rho - p)\right]. \tag{3.93}$$

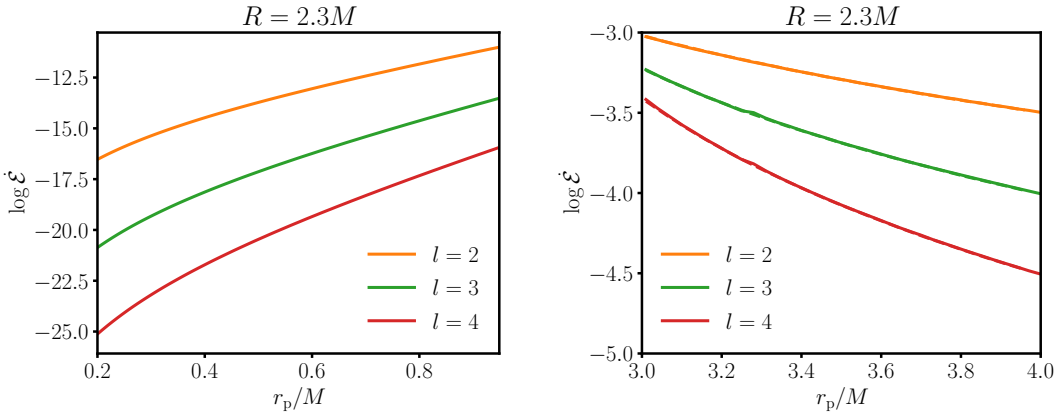

Figure 3.7: Axial electromagnetic radiation emitted by particles orbiting in the spacetime of a uniform-density star. The radiation is dominated by $l = 2$ mode. As particles get close to the light ring, regardless the stable or unstable one, the flux converges to a certain value. Excitations by particles near unstable light ring are negligible.

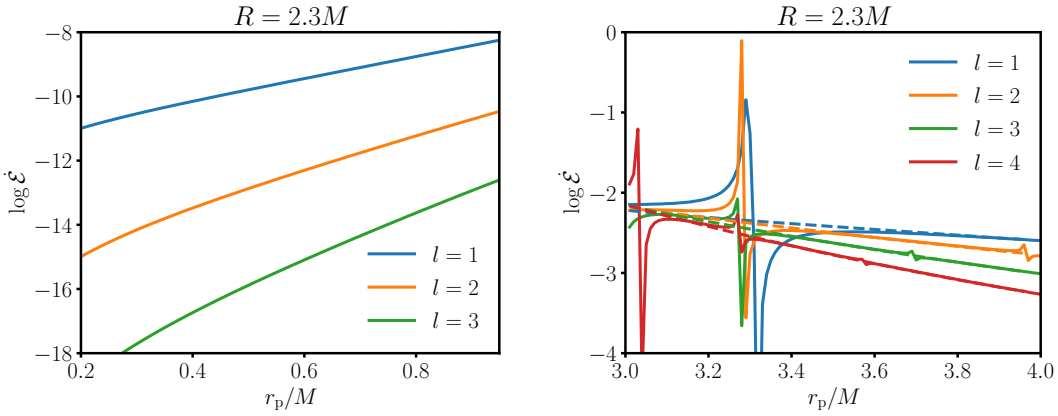

Figure 3.8: Polar electromagnetic radiation emitted by particles orbiting in the spacetime of a uniform-density star. Except for those excitations, polar radiation is significantly larger than axial radiation, and is the same as that in a Schwarzschild BH case (shown in dashed lines).

For circular motions, the source terms is given by

$$S_{\rm g} = \frac{8\sqrt{2}\pi i m_{\rm p} f^{\frac{3}{2}}(r) g^{\frac{1}{2}}(r) r}{\sqrt{l(l-1)(l+1)(l+2)}} \left[\frac{f'(r)}{f(r)} D_{lm}(r) + D'_{lm}(r) \right], \tag{3.94}$$

where

$$D_{lm}(r) = \frac{\sqrt{2} u_{\rm p} \Omega_{\rm p}^2 m \frac{\partial Y_{lm}}{\partial \theta}}{\sqrt{l(l-1)(l+1)(l+2)}} \frac{g^{\frac{1}{2}}(r)}{f^{\frac{1}{2}}(r)} \delta(r - r_{\rm p}). \tag{3.95}$$

And the energy flux is computed from

$$\dot{E}_{\rm g} = \frac{1}{16\pi} \frac{(l+2)!}{(l-2)!} |Z_{\rm g}|^2. \tag{3.96}$$

The polar radiation couples with the matter oscillation and is more complicated to deal, which is thus beyond the scope of this thesis.

Numerical results are presented in Figure 3.9. The flux is dominated by lower l modes and diverges at both stable and unstable light ring. The outside excitations are tiny, similar to that in the case of axial electromagnetic radiation.

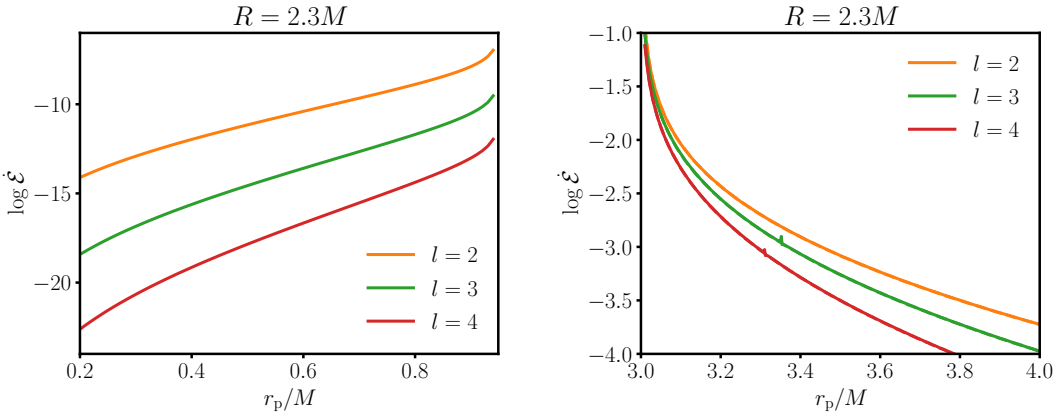

Figure 3.9: Axial gravitational radiation emitted by particles orbiting in the spacetime of a uniform-density star. The radiation is dominated by $l = 2$ mode and diverges at both stable and unstable light ring. Only weak excitations can be found near the outside light ring, similar to the axial electromagnetic radiation.

Chapter 4

Conclusions

In this thesis, we study both null and time-like geodesics in the spacetime of uniform-density stars, and geodesic synchrotron radiations emitted by particles orbiting circularly near stable and unstable light rings. Conclusions are summarised below:

- A sufficiently compact uniform-density star hosts two light rings: an unstable light ring at $r = r_+ = 3M$ and a stable light ring at $r = r_-$. The radius of the stable light ring is dependent on the compactness of the star. Due to the local valley of null geodesic potential, photons can be completely trapped inside the star, their orbits are all found to be closed. Stable circular time-like geodesics are allowed inside the stable light ring. Due to the lack of horizon and the assumption that the particles do not interact with the stellar matter, time-like particles can stably travel between the stable and unstable light rings.

- Scalar synchrotron radiation emitted by particles orbiting around the stable and unstable light rings is studied in both numerical and analytical approaches. Outside the star, apart from the excitations due to trapped modes, the scalar radiation is similar to that in the case of Schwarzschild BH: near the unstable light ring, the radiation is suppressed and dominated by high-frequency modes. For less compact stars, excitations only appear in high-frequency. Inside the star, no excitation is found, the radiation is dominated by low-frequency modes and suppressed neat the stable light ring. Comparing to the radiation emitted from unstable light ring, the flux emitted by particles orbiting around the stable light ring is also suppressed. Such suppression is less significant for less compact stars.

- The analytical result reveals that the suppression is due to the potential barrier between the stable light ring and turning point, since it contributes an exponential decreasing term. The suppression is manifested in two ways. On one hand, the existence of the potential barrier suppresses the flux emitted by particles orbiting

the stable light ring. On the other hand, as the barrier is proportional to the mode index l, the higher-frequency modes are also suppressed.

- Electromagnetic radiation and axial gravitational radiation are only computed in a numerical way, as the analytical expression do not provide a good approximation. Electromagnetic radiation converges to a certain value at both light rings, while axial gravitational radiation diverges at both light rings. Outside the star, excitations are also found, except which the radiations are the same as those in the Schwarzschild BH case. Radiations from the stable light ring are similarly suppressed.

As the gravitational radiation diverges at the stable light ring, at least for axial radiation, such radiation can be hopefully detected and be evidence for the existence of stable light rings. Future works shall first investigate polar gravitational radiation, which is likely to be more significant than axial radiation. Orbital evolution and gravitational waveform are also of interest. Additional, since uniform-density star is an idealized model, it is essential to study radiation from other more realistic ECO models such as boson star.

Appendix A

Photon escaping angle

Consider a static, spherically symmetric spacetime described by

$$\mathrm{d}s^2 = -f(r)\mathrm{d}t^2 + \frac{1}{g(r)}\mathrm{d}r^2 + r^2\mathrm{d}\Omega^2, \tag{A.1}$$

where $\mathrm{d}\Omega^2 = \mathrm{d}\theta^2 + \sin^2\theta\mathrm{d}\phi^2$. For the Schwarzschild geometry, $f(r) = g(r) = 1 - (2M/r)$.

In the equatorial plane $\theta = \pi/2$ and $\dot{\theta} = 0$, the motion of a photon can be described by,

$$0 = -f(r)\dot{t}^2 + \frac{1}{f(r)}\dot{r}^2 + r^2\dot{\phi}^2 \tag{A.2}$$

$$= -\frac{E^2}{f(r)} + \frac{1}{f(r)}\dot{r}^2 + \frac{L^2}{r^2}, \tag{A.3}$$

where the energy E and angular momentum L are respectively defined by

$$E = f(r)\dot{t}, \tag{A.4}$$

$$L = r^2\dot{\phi}. \tag{A.5}$$

Therefore, we have

$$\dot{r}^2 = E^2 - \frac{L^2}{r^2}f(r) = L^2\left[\frac{1}{b^2} - V(r)\right], \tag{A.6}$$

where

$$b = \frac{L}{E}, \tag{A.7}$$

$$V(r) = \frac{f(r)}{r^2} = \frac{1 - \frac{2M}{r}}{r^2}. \tag{A.8}$$

$V(r)$ reaches its maximum $V_{\max} = 1/(27M^2)$ at $r = 3M$ as $V'(3M) = 0$ and $V'(3M) < 0$. For a photon emitting outward at $2M < r < 3M$, if its $b > 3\sqrt{3}M$, it will reach the turning point, determined by $\dot{r}^2 = 0$, and then fall back into central object; if its

$b < 3\sqrt{3}M$, $\dot{r}^2$ will always be positive and the photon can escape to infinity. Therefore, a photon can only escape from the central object when $b = L/E < 3\sqrt{3}M$. The case of $b = 3\sqrt{3}M$ represents the critical orbit.

For an observer fixed at r, the locally measured tangential velocity of photon is

$$v_\phi = \frac{r\mathrm{d}\phi}{\mathrm{d}\tilde{t}} \tag{A.9}$$

$$= \frac{r\mathrm{d}\phi}{\sqrt{f(r)}\mathrm{d}t} \tag{A.10}$$

$$= \frac{b}{r}\sqrt{f(r)}. \tag{A.11}$$

Therefore, for an escaping photon, the angle ψ between the emitting direction and r-direction satisfies

$$\sin\psi = v_\phi = \frac{b}{r}\sqrt{1-\frac{2M}{r}} < \frac{3\sqrt{3}M}{r}\sqrt{1-\frac{2M}{r}}, \tag{A.12}$$

corresponding to a solid angle of

$$\Delta\Omega = 2\pi(1-\cos\psi) = 2\pi\left[1-\sqrt{1-\frac{27M^2(r-2M)}{r^3}}\right]. \tag{A.13}$$

At $r_0 = 2M(1+\epsilon)$, the escaping angle and the corresponding solid angle are respectively

$$\sin\psi_{\mathrm{esc}} = \frac{3\sqrt{3}}{2(1+\epsilon)}\sqrt{1-\frac{1}{1+\epsilon}} = \frac{3\sqrt{3}}{2}\sqrt{\epsilon} + \mathcal{O}(\epsilon^{\frac{3}{2}}), \tag{A.14}$$

$$\Delta\Omega_{\mathrm{esc}} = 2\pi\left(1-\sqrt{1-\frac{27\epsilon}{4(1+\epsilon)^3}}\right) = \frac{27\pi}{4}\epsilon + \mathcal{O}(\epsilon^2). \tag{A.15}$$

A turning-back photon reaches its maximum distance when $1/b^2 = f(r_{\mathrm{max}})/r_{\mathrm{max}}^2$, so that

$$r_{\mathrm{max}} = 2M + \frac{8}{b^2}M^3 + \mathcal{O}(M^5) \tag{A.16}$$

$$\approx 2M(1+\frac{4f_0M^2}{r_0^2\sin^2\psi}), \tag{A.17}$$

where $f_0 \equiv f(r_0) = 1-(2M/r_0)$.

Appendix B

Particle collisions at the surface

Consider a static, spherically symmetric spacetime described by

$$\mathrm{d}s^2 = -f(r)\mathrm{d}t^2 + \frac{1}{g(r)}\mathrm{d}r^2 + r^2\mathrm{d}\Omega^2, \tag{B.1}$$

where $\mathrm{d}\Omega^2 = \mathrm{d}\theta^2 + \sin^2\theta\mathrm{d}\phi^2$. For the Schwarzschild geometry, $f(r) = g(r) = 1 - (2M/r)$.

For an infalling particle, its four-velocity is

$$v^\mu_{(1)} = \left(\frac{E}{f}, -\sqrt{E^2 - f\left(\frac{L^2}{r^2} + 1\right)}, \frac{L}{r^2}, 0\right), \tag{B.2}$$

where E and L are respectively the specific energy and angular momentum of the falling particle. For a particle rest at the surface of an ECO $R = 2M(1+\epsilon)$, its four-velocity is

$$v^\mu_{(2)} = \left(\frac{1}{\sqrt{f}}, 0, 0, 0\right). \tag{B.3}$$

Consider the collision between an infalling particle and a particle rest at the surface and both particles have a rest mass m_0, their center-of-mass energy for collision is

$$E_{\mathrm{CM}} = m_0\sqrt{2}\sqrt{1 - g_{\mu\nu}v^\mu_{(1)}v^\nu_{(2)}}, \tag{B.4}$$

$$= m_0\sqrt{2}\sqrt{1 + \frac{E}{f^{3/2}}}, \tag{B.5}$$

$$= m_0\sqrt{2}\sqrt{1 + \frac{E}{\sqrt{1 - \frac{1}{1+\epsilon}}}}, \tag{B.6}$$

$$= m_0\sqrt{2}\left[\frac{\sqrt{E}}{\epsilon^{1/4}} + \mathcal{O}(\epsilon^{1/4})\right]. \tag{B.7}$$

The expression for the collision energy Eq.(B.4) is justified as follows.

Consider a two-particle system in a flat spacetime, their four-momentums are defined as $P_{(1)} = (E_{(1)}, \boldsymbol{p}_{(1)})$ and $P_{(2)} = (E_{(2)}, \boldsymbol{p}_{(2)})$, and the total four-momentum of the system is

$P = P_{(1)} + P_{(2)} = (E_{(1)} + E_{(2)}, \boldsymbol{p}_{(1)} + \boldsymbol{p}_{(2)})$. In the conter-of-mass frame, the total energy is $E_{\rm CM}$ and the total four-momentum is thus $P_{\rm CM} = (E_{\rm CM}, \mathbf{0})$. The squared four-momentum is Lorentz invariant, therefore

$$E_{\rm CM}^2 = (E_{(1)} + E_{(2)})^2 - (\boldsymbol{p}_{(1)} + \boldsymbol{p}_{(2)})^2 \tag{B.8}$$
$$= (E_{(1)}^2 - p_{(1)}^2) + (E_{(2)}^2 - p_{(2)}^2) + 2(E_{(1)}E_{(2)} - \boldsymbol{p}_{(1)} \cdot \boldsymbol{p}_{(2)}) \tag{B.9}$$
$$= m_{(1)}^2 + m_{(2)}^2 - 2\eta_{\alpha\beta} P_{(1)}^\alpha P_{(2)}^\beta \tag{B.10}$$
$$= m_{(1)}^2 + m_{(2)}^2 - 2m_{(1)}m_{(2)}\eta_{\alpha\beta} v_{(1)}^\alpha v_{(2)}^\beta, \tag{B.11}$$

where $\eta_{\alpha\beta}$ is the Minkowski metric and $\mathrm{diag}(\eta_{\alpha\beta}) = (-1, 1, 1, 1)$. For a curved spacetime described by the metric $g_{\mu\nu}$, one can always find a local inertial system that the above equation holds valid. As long as $g_{\mu\nu}$ is known, the coordinate transformation is well defined, and thus $v^\alpha = \frac{\partial x^\alpha}{\partial x^\mu} v^\mu$ and $g_{\mu\nu} = \frac{\partial x^\alpha}{\partial x^\mu}\frac{\partial x^\beta}{\partial x^\nu}\eta_{\mu\nu}$. The center-of-mass energy becomes

$$E_{\rm CM}^2 = m_{(1)}^2 + m_{(2)}^2 - 2m_{(1)}m_{(2)}\eta_{\alpha\beta} v_{(1)}^\alpha v_{(2)}^\beta \tag{B.12}$$
$$= m_{(1)}^2 + m_{(2)}^2 - 2m_{(1)}m_{(2)}\eta_{\alpha\beta}\frac{\partial x^\alpha}{\partial x^\mu} v_{(1)}^\mu \frac{\partial x^\beta}{\partial x^\nu} v_{(2)}^\nu \tag{B.13}$$
$$= m_{(1)}^2 + m_{(2)}^2 - 2m_{(1)}m_{(2)} g_{\mu\nu} v_{(1)}^\mu v_{(2)}^\nu. \tag{B.14}$$

For $m_{(1)} = m_{(2)} = m_0$, the expression of $E_{\rm CM}$ is therefore

$$E_{\rm CM}^2 = 2m_0^2 - 2m_0^2 g_{\mu\nu} v_{(1)}^\mu v_{(2)}^\nu \tag{B.15}$$
$$= 2m_0^2(1 - g_{\mu\nu} v_{(1)}^\mu v_{(2)}^\nu). \tag{B.16}$$

Appendix C

Bound orbits revisited

The original purpose of the introduction to q is to describe the bound orbits of time-like particles [75], we believe it is still valid when we extend it to describe the bound orbits of photons. However, a few things will be different, at least in our case of constant-density star.

Zoom-whirl behaviour is not necessary. —— For time-like particles, zoom-whirl behaviour is unavoidable in the region of strong gravitational field. It means the particles whirls around the central BH before zooming out. For photons trapped inside the unstable light ring, zoom-whirl behaviour seems not necessary. As shown in Figure 2.3, one can find in the case of $b = 5.197M$ there is an extra whirl before the photon travels to its pericenter, corresponding to $q \gtrsim 1$, but in $b = 5.6M$ and $b = 6.2M$ cases, there is no extra whirl, the orbits look more like precessing orbits of planets, corresponding to $0 < q \ll 1$.

Allowed range of q. —— For $b \to b_R$, the photon travels around near the unstable light ring for an infinity time before it falls into the star, therefore $\Delta\phi \to +\infty$ and $q \to +\infty$. This is similar to when a time-like particle travels its unstable circular orbit. But we need to be careful when determine the lower limit of q. According to its definition, the q value of a closed, ellipse-like orbit is zero. In principle, lower values of q with $|q| \ll 1$ are acceptable, they correspond to retrograde precession. But when $|q|$ becomes larger, the orbit can be impossible. $q = -\frac{1}{2}$ makes $\Delta\phi = \pi$ and $\int_{r_-}^{r_+} \frac{\mathrm{d}\phi}{\mathrm{d}r}\,\mathrm{d}r = \pi/2$, implying that the accumulated azimuth between two turning points is $\pi/2$. This orbit would look like a peanut shell, which could not exist in a single-source gravitational field.

All orbits inside the star are closed. —— As stated above, we find $q \to 0$ when $b \to b_R$ and $q = 0$ for $b_R < b < b_-$. The most solid way to draw this conclusion is to calculate the integral $\int_{r_-}^{r_+} \frac{\mathrm{d}\phi}{\mathrm{d}r}\,\mathrm{d}r$ analytically and prove it equals to π. But it seems unrealistic due to complexity of the expressions for $r_{+,-}$. One cannot obtain a perfectly exact result in numerical calculation. And the numerical result q_{num} is always smaller than its true value q_{true}. We cannot start the integral from r_- exactly because $\frac{\mathrm{d}\phi}{\mathrm{d}r}$ diverges at this point. Therefore, we can only obtain the accumulated azimuth between $[r_- + \delta, r_+ - \delta]$ with

$\delta \ll 1$, ending up with a smaller q. When $\delta \to 0$, $q_{\rm num}$ tends to the true value $q_{\rm true}$. In Figure C.1, we display our results of q with various δ, note that all these values of q are negative thus the y-axis is $\log|q|$. As δ decreases, the values of $q_{\rm num}$ become closer to zero. Hence, we conclude all values of $q_{\rm true}$ for $b_R < b < b_-$ equal to zero, implying closed orbits. When $b \to b_-$, q seems to tend to decrease. We claim that this is caused by the disadvantage of numerical calculation. Near the pericenter r_-, r increases slowly, leading to a large value of $\frac{\mathrm{d}\phi}{\mathrm{d}r}$. This effect becomes much more significant when the orbit gets close to the stable light ring. As a result, the accumulated azimuth between r_- and $r_- + \delta$ increases rapidly and causes what we find in the right of Figure C.1. Based on the discussion above, it is natural to deduce that $q = 0$ at $b = b_R$, where the orbit just touches the surface of star, and at $b = b_-$, the stable circular orbit – the stable light ring. For now, we are not sure whether this is a unique property of constant-density star or a general property of ultracompact objects, we expect further calculation can bring answers.

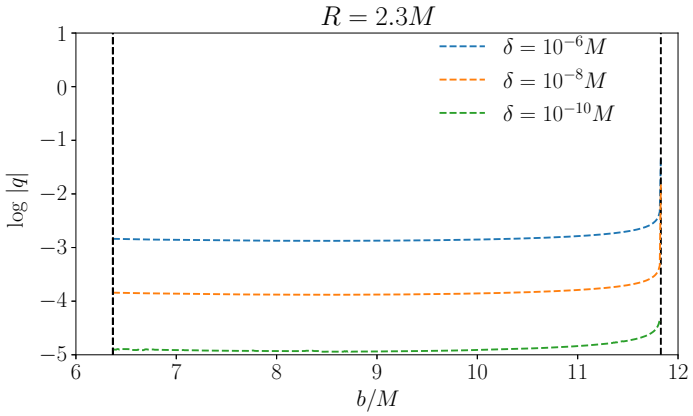

Figure C.1: Curves of $\log|q|$ for $b_R < b < b_-$, with different choices of δ. The star radius is fixed as $R = 2.3M$. Note that all the q are negative in this figure.

Bibliography

[1] Karl Schwarzschild. On the gravitational field of a mass point according to Einstein's theory. *Sitzungsber. Preuss. Akad. Wiss. Berlin (Math. Phys.)*, 1916:189–196, 1916.

[2] Roy P. Kerr. Gravitational Field of a Spinning Mass as an Example of Algebraically Special Metrics. *Phys. Rev. Lett.*, 11(5):237–238, September 1963.

[3] Ramesh Narayan. Black holes in astrophysics. *New Journal of Physics*, 7(1):199, September 2005.

[4] B. Carter. Axisymmetric Black Hole Has Only Two Degrees of Freedom. *Phys. Rev. Lett.*, 26(6):331–333, February 1971.

[5] B.P. Abbott et al. Observation of Gravitational Waves from a Binary Black Hole Merger. *Phys. Rev. Lett.*, 116(6):061102, 2016.

[6] B.P. Abbott et al. Binary Black Hole Mergers in the first Advanced LIGO Observing Run. *Phys. Rev. X*, 6(4):041015, 2016. [Erratum: Phys.Rev.X 8, 039903 (2018)].

[7] B.P. Abbott et al. GW170814: A Three-Detector Observation of Gravitational Waves from a Binary Black Hole Coalescence. *Phys. Rev. Lett.*, 119(14):141101, 2017.

[8] B.P. Abbott et al. GWTC-1: A Gravitational-Wave Transient Catalog of Compact Binary Mergers Observed by LIGO and Virgo during the First and Second Observing Runs. *Phys. Rev. X*, 9(3):031040, 2019.

[9] R. Abbott et al. GWTC-2: Compact Binary Coalescences Observed by LIGO and Virgo During the First Half of the Third Observing Run. *Phys. Rev. X*, 11:021053, 2021.

[10] R. Abbott et al. Observation of gravitational waves from two neutron star-black hole coalescences. *Astrophys. J. Lett.*, 915:L5, 2021.

[11] Event Horizon Telescope Collaboration. First M87 Event Horizon Telescope Results. I. The Shadow of the Supermassive Black Hole. *Astrophys. J. Lett.*, 875(1):L1, April 2019.

[12] Event Horizon Telescope Collaboration. First M87 Event Horizon Telescope Results. II. Array and Instrumentation. *Astrophys. J. Lett.*, 875(1):L2, April 2019.

[13] Event Horizon Telescope Collaboration. First M87 Event Horizon Telescope Results. III. Data Processing and Calibration. *Astrophys. J. Lett.*, 875(1):L3, April 2019.

[14] Event Horizon Telescope Collaboration. First M87 Event Horizon Telescope Results. IV. Imaging the Central Supermassive Black Hole. *Astrophys. J. Lett.*, 875(1):L4, April 2019.

[15] Event Horizon Telescope Collaboration. First M87 Event Horizon Telescope Results. V. Physical Origin of the Asymmetric Ring. *Astrophys. J. Lett.*, 875(1):L5, April 2019.

[16] Event Horizon Telescope Collaboration. First M87 Event Horizon Telescope Results. VI. The Shadow and Mass of the Central Black Hole. *Astrophys. J. Lett.*, 875(1):L6, April 2019.

[17] EHT Collaboration. First Sagittarius A* Event Horizon Telescope Results. I. The Shadow of the Supermassive Black Hole in the Center of the Milky Way. *Astrophys. J. Lett.*, 930(2):L12, May 2022.

[18] EHT Collaboration. First Sagittarius A* Event Horizon Telescope Results. II. EHT and Multiwavelength Observations, Data Processing, and Calibration. *Astrophys. J. Lett.*, 930(2):L13, May 2022.

[19] EHT Collaboration. First Sagittarius A* Event Horizon Telescope Results. III. Imaging of the Galactic Center Supermassive Black Hole. *Astrophys. J. Lett.*, 930(2):L14, May 2022.

[20] EHT Collaboration. First Sagittarius A* Event Horizon Telescope Results. IV. Variability, Morphology, and Black Hole Mass. *Astrophys. J. Lett.*, 930(2):L15, May 2022.

[21] EHT Collaboration. First Sagittarius A* Event Horizon Telescope Results. V. Testing Astrophysical Models of the Galactic Center Black Hole. *Astrophys. J. Lett.*, 930(2):L16, May 2022.

[22] EHT Collaboration. First Sagittarius A* Event Horizon Telescope Results. VI. Testing the Black Hole Metric. *Astrophys. J. Lett.*, 930(2):L17, May 2022.

[23] Raúl Carballo-Rubio, Francesco Di Filippo, Stefano Liberati, and Matt Visser. Phenomenological aspects of black holes beyond general relativity. *Phys. Rev. D*, 98(12):124009, December 2018.

[24] Sean A. Hayward. Formation and Evaporation of Nonsingular Black Holes. *Phys. Rev. Lett.*, 96(3):031103, January 2006.

[25] Shao-Wen Wei, Yu-Xiao Liu, and Chun-E. Fu. Null Geodesics and Gravitational Lensing in a Nonsingular Spacetime. *Advances in High Energy Physics*, 2015:1, January 2015.

[26] Shan-Shan Zhao and Yi Xie. Strong deflection gravitational lensing by a modified Hayward black hole. *European Physical Journal C*, 77(5):272, May 2017.

[27] Ahmadjon Abdujabbarov, Muhammed Amir, Bobomurat Ahmedov, and Sushant G. Ghosh. Shadow of rotating regular black holes. *Phys. Rev. D*, 93(10):104004, May 2016.

[28] Vitor Cardoso and Paolo Pani. Testing the nature of dark compact objects: a status report. *Living Reviews in Relativity*, 22(1):4, July 2019.

[29] I. D. Novikov and K. S. Thorne. Astrophysics and black holes. In *Les Houches Summer School of Theoretical Physics: Black Holes*, pages 343–550, 1973.

[30] Avery E. Broderick and Abraham Loeb. Imaging bright spots in the accretion flow near the black hole horizon of Sgr A*. *Mon. Not. Roy. Astron. Soc.*, 363:353–362, 2005.

[31] Avery E. Broderick and Abraham Loeb. Imaging optically-thin hot spots near the black hole horizon of sgr a* at radio and near-infrared wavelengths. *Mon. Not. Roy. Astron. Soc.*, 367:905–916, 2006.

[32] S. Chandrasekhar. *The mathematical theory of black holes*. 1983.

[33] F. H. Vincent, Z. Meliani, P. Grandclément, E. Gourgoulhon, and O. Straub. Imaging a boson star at the Galactic center. *Classical and Quantum Gravity*, 33(10):105015, May 2016.

[34] Vitor Cardoso, Luís C. B. Crispino, Caio F. B. Macedo, Hirotada Okawa, and Paolo Pani. Light rings as observational evidence for event horizons: long-lived modes, ergoregions and nonlinear instabilities of ultracompact objects. *Phys. Rev. D*, 90(4):044069, 2014.

[35] Caio F. B. Macedo, Paolo Pani, Vitor Cardoso, and Luís C. B. Crispino. Astrophysical signatures of boson stars: Quasinormal modes and inspiral resonances. *Phys. Rev. D*, 88:064046, Sep 2013.

[36] Pedro V. P. Cunha, Emanuele Berti, and Carlos A. R. Herdeiro. Light-ring stability for ultracompact objects. *Phys. Rev. Lett.*, 119:251102, Dec 2017.

[37] Gianfranco Bertone and Tim M. P. Tait. A new era in the search for dark matter. *Nature*, 562(7725):51–56, October 2018.

[38] Gianfranco Bertone and Dan Hooper. History of dark matter. *Reviews of Modern Physics*, 90(4):045002, October 2018.

[39] J. G. de Swart, G. Bertone, and J. van Dongen. How dark matter came to matter. *Nature Astronomy*, 1:0059, March 2017.

[40] Gaurav Narain, Jürgen Schaffner-Bielich, and Igor N. Mishustin. Compact stars made of fermionic dark matter. *Phys. Rev. D*, 74(6):063003, September 2006.

[41] Martti Raidal, Sergey Solodukhin, Ville Vaskonen, and Hardi Veermäe. Light primordial exotic compact objects as all dark matter. *Phys. Rev. D*, 97(12):123520, June 2018.

[42] Maksym Deliyergiyev, Antonino Del Popolo, Laura Tolos, Morgan Le Delliou, Xiguo Lee, and Fiorella Burgio. Dark compact objects: An extensive overview. *Phys. Rev. D*, 99(6):063015, March 2019.

[43] Edward Seidel and Wai-Mo Suen. Formation of solitonic stars through gravitational cooling. *Phys. Rev. Lett.*, 72(16):2516–2519, April 1994.

[44] Steven L. Liebling and Carlos Palenzuela. Dynamical boson stars. *Living Reviews in Relativity*, 26(1):1, December 2023.

[45] Richard Brito, Vitor Cardoso, and Hirotada Okawa. Accretion of Dark Matter by Stars. *Phys. Rev. Lett.*, 115(11):111301, September 2015.

[46] Fabrizio Di Giovanni, Nicolas Sanchis-Gual, Carlos A. R. Herdeiro, and José A. Font. Dynamical formation of Proca stars and quasistationary solitonic objects. *Phys. Rev. D*, 98(6):064044, September 2018.

[47] Philippe Grandclément. Light rings and light points of boson stars. *Phys. Rev. D*, 95(8):084011, April 2017.

[48] Monica Colpi, Stuart L. Shapiro, and Ira Wasserman. Boson stars: Gravitational equilibria of self-interacting scalar fields. *Phys. Rev. Lett.*, 57(20):2485–2488, November 1986.

[49] R. Friedberg, T. D. Lee, and Y. Pang. Scalar soliton stars and black holes. *Phys. Rev. D*, 35(12):3658–3677, June 1987.

[50] Lam Hui, Jeremiah P. Ostriker, Scott Tremaine, and Edward Witten. Ultralight scalars as cosmological dark matter. *Phys. Rev. D*, 95(4):043541, February 2017.

[51] Andrea Maselli, Pantelis Pnigouras, Niklas Grønlund Nielsen, Chris Kouvaris, and Kostas D. Kokkotas. Dark stars: Gravitational and electromagnetic observables. *Phys. Rev. D*, 96:023005, Jul 2017.

[52] C. J. Horowitz and Sanjay Reddy. Gravitational Waves from Compact Dark Objects in Neutron Stars. *Phys. Rev. Lett.*, 122(7):071102, February 2019.

[53] John Ellis, Andi Hektor, Gert Hütsi, Kristjan Kannike, Luca Marzola, Martti Raidal, and Ville Vaskonen. Search for dark matter effects on gravitational signals from neutron star mergers. *Physics Letters B*, 781:607–610, June 2018.

[54] Máximo Bañados, Joseph Silk, and Stephen M. West. Kerr Black Holes as Particle Accelerators to Arbitrarily High Energy. *Phys. Rev. Lett.*, 103(11):111102, September 2009.

[55] S. R. Kelner, F. A. Aharonian, and V. V. Bugayov. Energy spectra of gamma rays, electrons, and neutrinos produced at proton-proton interactions in the very high energy regime. *Phys. Rev. D*, 74:034018, Aug 2006.

[56] C. W. Misner. Interpretation of Gravitational-Wave Observations. *Phys. Rev. Lett.*, 28(15):994–997, April 1972.

[57] C. W. Misner, R. A. Breuer, D. R. Brill, P. L. Chrzanowski, H. G. Hughes, and C. M. Pereira. Gravitational Synchrotron Radiation in the Schwarzschild Geometry. *Phys. Rev. Lett.*, 28(15):998–1001, April 1972.

[58] R. A. Breuer, R. Ruffini, J. Tiomno, and C. V. Vishveshwara. Vector and Tensor Radiation from Schwarzschild Relativistic Circular Geodesics. *Phys. Rev. D*, 7(4):1002–1007, February 1973.

[59] Marc Davis, Remo Ruffini, Jayme Tiomno, and Frank Zerilli. Can Synchrotron Gravitational Radiation Exist? *Phys. Rev. Lett.*, 28(20):1352–1355, May 1972.

[60] João P. B. Brito, Rafael P. Bernar, and Luís C. B. Crispino. Synchrotron geodesic radiation in Schwarzschild-de Sitter spacetime. *Phys. Rev. D*, 101(12):124019, June 2020.

[61] Vitor Cardoso and José P. Lemos. Scalar synchrotron radiation in the Schwarzschild-anti-de Sitter geometry. *Phys. Rev. D*, 65(10):104033, May 2002.

[62] Pau Amaro-Seoane, Heather Audley, Stanislav Babak, John Baker, Enrico Barausse, Peter Bender, Emanuele Berti, Pierre Binetruy, Michael Born, Daniele Bortoluzzi, Jordan Camp, Chiara Caprini, Vitor Cardoso, Monica Colpi, John Conklin, Neil Cornish, Curt Cutler, Karsten Danzmann, Rita Dolesi, Luigi Ferraioli, Valerio Ferroni, Ewan Fitzsimons, Jonathan Gair, Lluis Gesa Bote, Domenico Giardini, Ferran Gibert, Catia Grimani, Hubert Halloin, Gerhard Heinzel, Thomas Hertog, Martin Hewitson, Kelly Holley-Bockelmann, Daniel Hollington, Mauro Hueller, Henri Inchauspe, Philippe Jetzer, Nikos Karnesis, Christian Killow, Antoine Klein, Bill Klipstein, Natalia Korsakova, Shane L Larson, Jeffrey Livas, Ivan Lloro, Nary Man, Davor Mance, Joseph Martino, Ignacio Mateos, Kirk McKenzie, Sean T McWilliams, Cole Miller, Guido Mueller, Germano Nardini, Gijs Nelemans, Miquel Nofrarias, Antoine Petiteau, Paolo Pivato, Eric Plagnol, Ed Porter, Jens Reiche, David Robertson, Norna Robertson, Elena Rossi, Giuliana Russano, Bernard Schutz, Alberto Sesana, David Shoemaker, Jacob Slutsky, Carlos F. Sopuerta, Tim Sumner, Nicola Tamanini, Ira Thorpe, Michael Troebs, Michele Vallisneri, Alberto Vecchio, Daniele Vetrugno, Stefano Vitale, Marta Volonteri, Gudrun Wanner, Harry Ward, Peter Wass, William Weber, John Ziemer, and Peter Zweifel. Laser Interferometer Space Antenna. *arXiv e-prints*, page arXiv:1702.00786, February 2017.

[63] Stanislav Babak, Jonathan Gair, Alberto Sesana, Enrico Barausse, Carlos F. Sopuerta, Christopher P. L. Berry, Emanuele Berti, Pau Amaro-Seoane, Antoine Petiteau, and Antoine Klein. Science with the space-based interferometer lisa. v. extreme mass-ratio inspirals. *Phys. Rev. D*, 95:103012, May 2017.

[64] Enrico Barausse, Emanuele Berti, Vitor Cardoso, Scott A. Hughes, and Gaurav Khanna. Divergences in gravitational-wave emission and absorption from extreme mass ratio binaries. *Phys. Rev. D*, 104(6):064031, September 2021.

[65] Karl Schwarzschild. Über das Gravitationsfeld einer Kugel aus inkompressibler Flüssigkeit nach der Einsteinschen Theorie. In *Sitzungsberichte der Königlich Preussischen Akademie der Wissenschaften zu Berlin*, pages 424–434, March 1916.

[66] Arthur Stanley Eddington. *The mathematical theory of relativity*. Cambridge Univ. Press, 1923.

[67] Steven Weinberg. *Gravitation and Cosmology: Principles and Applications of the General Theory of Relativity*. John Wiley and Sons, 1972.

[68] Stuart L. Shapiro and Saul A. Teukolsky. *Black holes, white dwarfs, and neutron stars : the physics of compact objects*. John Wiley & Sons, Ltd, 1983.

[69] K. D. Krori and P. Borgohain. Uniform-density cold neutron stars in general relativity. *Journal of Physics A Mathematical General*, 8(4):512–520, April 1975.

[70] Nils Andersson, Yasufumi Kojima, and Kostas D. Kokkotas. On the Oscillation Spectra of Ultracompact Stars: an Extensive Survey of Gravitational-Wave Modes. *Astrophys. J.*, 462:855, May 1996.

[71] Nils Andersson and Kostas D. Kokkotas. Gravitational Waves and Pulsating Stars: What Can We Learn from Future Observations? *Phys. Rev. Lett.*, 77(20):4134–4137, November 1996.

[72] K. D. Kokkotas and N. Stergioulas. Analytic description of the r-mode instability in uniform density stars. *Astron. Astrophys.*, 341:110–116, January 1999.

[73] Abhas Mitra. No uniform density star in general relativity. *Astrophys. Space Sci.*, 333(1):169–174, May 2011.

[74] H. A. Buchdahl. General relativistic fluid spheres. *Phys. Rev.*, 116:1027–1034, Nov 1959.

[75] Janna Levin and Gabe Perez-Giz. A Periodic Table for Black Hole Orbits. *Phys. Rev. D*, 77:103005, 2008.

[76] R. A. Breuer, P. L. Chrzanowksi, H. G. Hughes, and C. W. Misner. Geodesic Synchrotron Radiation. *Phys. Rev. D*, 8(12):4309–4319, December 1973.

[77] Vitor Cardoso, Adrián del Río, and Masashi Kimura. Distinguishing black holes from horizonless objects through the excitation of resonances during inspiral. *Phys. Rev. D*, 100(8):084046, October 2019.

[78] Yasufumi Kojima, Nils Andersson, and Kostas D. Kokkotas. On the Oscillation Spectra of Ultra Compact Stars. *Proceedings of the Royal Society of London Series A*, 451(1942):341–348, November 1995.

[79] Kostas D. Kokkotas and Bernd G. Schmidt. Quasi-Normal Modes of Stars and Black Holes. *Living Reviews in Relativity*, 2(1):2, September 1999.

[80] Paolo Pani. Advanced Methods in Black-Hole Perturbation Theory. *Int. J. Mod. Phys. A*, 28:1340018, 2013.

[81] F. J. Zerilli. Perturbation analysis for gravitational and electromagnetic radiation in a reissner-nordstroem geometry. *Phys. Rev. D*, 9:860–868, 1974.

[82] Vitor Cardoso, Caio F. B. Macedo, Paolo Pani, and Valeria Ferrari. Black holes and gravitational waves in models of minicharged dark matter. *J. Cosmol. Astropart. Phys.*, 2016(5):054, May 2016.

[83] Kip S. Thorne and Alfonso Campolattaro. Non-Radial Pulsation of General-Relativistic Stellar Models. I. Analytic Analysis for L >= 2. Astrophysical Journal, vol. 149, p.591, September 1967.

[84] Tullio Regge and John A. Wheeler. Stability of a Schwarzschild singularity. *Phys. Rev.*, 108:1063–1069, 1957.

[85] Frank J. Zerilli. Effective potential for even parity Regge-Wheeler gravitational perturbation equations. *Phys. Rev. Lett.*, 24:737–738, 1970.

[86] Norichika Sago, Hiroyuki Nakano, and Misao Sasaki. Gauge problem in the gravitational selfforce. 1. Harmonic gauge approach in the Schwarzschild background. *Phys. Rev.*, D67:104017, 2003.